

1 **FIRST MOMENTS OF A POLYHEDRON CLIPPED BY A**
2 **PARABOLOID***

3 FABIEN EVRARD^{†‡}, ROBERT CHIODI[§], AUSTIN HAN[‡], BEREND VAN WACHEM[†],
4 AND OLIVIER DESJARDINS[‡]

5 **Abstract.** We provide closed-form expressions for the first moments (i.e., the volume and
6 volume-weighted centroid) of a polyhedron clipped by a paraboloid, that is, of a polyhedron inter-
7 sected with the subset of the three-dimensional real space located on one side of a paraboloid. These
8 closed-form expressions are derived following successive applications of the divergence theorem and
9 the judicious parametrization of the intersection of the polyhedron's faces with the paraboloid. We
10 provide means for identifying ambiguous discrete intersection topologies, and propose a corrective
11 procedure for preventing their occurrence. Finally, we put our proposed closed-form expressions and
12 numerical approach to the test with millions of random and manually engineered polyhedron/parab-
13 loid intersection configurations. The results of these tests show that we are able to provide robust
14 machine-accurate estimates of the first moments at a computational cost that is within one order of
15 magnitude of that of state-of-the-art half-space clipping algorithms.

16 **Key words.** paraboloid, polyhedron, moments, volume, centroid, clipping, intersection

17 **AMS subject classifications.** 28-04, 28-08, 52B99, 58C99

18 **1. Introduction.** Many computational methods and applications, ranging from
19 finite-element [26, 5], cut-cell discontinuous Galerkin [12], and immersed isometric
20 analysis methods [18, 3], to the initialization [4, 19, 21, 22, 28] and transport [25] of
21 interfaces for simulating gas-liquid flows, require estimating integrals over polyhedra
22 that are clipped by curved surfaces. These applications have engendered multiple
23 dedicated quadrature rules and integration strategies, most of which focusing on esti-
24 mating the first few moments of these clipped polyhedra, thus considering polynomial
25 integrands only. The numerical approaches employed to estimate these moments vary
26 greatly in terms of accuracy, computational cost, and robustness. Monte-Carlo meth-
27 ods [13, 16] are extremely robust and straightforward to implement, however, they
28 suffer from a poor convergence rate, hence their cost/accuracy ratio is significant. Ap-
29 proaches based on octree subdivision [2, 23, 10] or surface triangulation/tesselation
30 [28] exhibit better convergence rates, yet their computational cost remains prohibitive
31 for numerical applications requiring *on-the-fly* moment estimations. A number of re-
32 cent approaches rely on successive applications of the divergence theorem, converting
33 the first moments of a clipped polyhedron into two- and/or one-dimensional integrals.
34 These integrals can then be numerically integrated at low computational cost or, for
35 specific surface types, even be derived into closed-form expressions. Bnà *et al.* [4] esti-
36 mate the volume (zeroth moment) of a cube clipped by an implicit surface represented
37 with a level-set function through integrating the local height of the surface using a
38 two-dimensional Gauss-Legendre quadrature rule. This work has been extended to
39 the first moments of a clipped cuboid by Chierici *et al.* [6]. For the similar pur-

[†]Lehrstuhl für Mechanische Verfahrenstechnik, Otto-von-Guericke-Universität Magdeburg, Uni-
versitätsplatz 2, 39106 Magdeburg, Germany.

[‡]Sibley School of Mechanical and Aerospace Engineering, Cornell University, Ithaca, NY 14853,
United States of America.

[§]Computer, Computational, and Statistical Sciences Division, Los Alamos National Laboratory,
Los Alamos, NM 87545, United States of America.

*Submitted to SIAM Journal on Scientific Computing

Funding: This project has received funding from the European Union's Horizon 2020 research
and innovation programme under the Marie Skłodowska-Curie grant agreement No 101026017.

40 pose of estimating the zeroth moment of a polyhedron clipped by an implicit surface,
 41 Jones *et al.* [19] decompose the clipped polyhedron into a set of simplices, themselves
 42 split into a reference polyhedron whose volume is computed analytically, and a set of
 43 fundamental curved domains whose volumes are estimated using a two-dimensional
 44 Gauss-Legendre quadrature rule. Chin and Sukumar [7] use a Duvanant quadrature
 45 rule [11] for integrating over the faces of a polyhedron bounded by rational or non-
 46 rational Bézier and B-spline patches. For non-rational surface parametrizations, this
 47 yields exact integral estimations of polynomial integrands, provided that the order of
 48 the Duvanant rule is high enough. Kromer and Bothe [21, 22] estimate the zeroth
 49 moment of a polyhedron clipped by an implicit surface by locally approximating the
 50 implicit surface as a paraboloid and applying the divergence theorem twice, converting
 51 the clipped volume into a sum of one-dimensional integrals, which are then estimated
 52 with a Gauss-Legendre quadrature rule. Finally, using Bernstein basis functions in-
 53 stead of monomial ones, Antolin and Hirschler [3] recently showed that, following
 54 successive applications of the divergence theorem, polynomial integrands can be in-
 55 tegrated in a straightforward and analytical manner over curved polyhedra bounded
 56 by non-rational Bézier or B-spline surfaces.

57 This manuscript is concerned with estimating the first moments of a specific type
 58 of curved polyhedra, that are planar non-convex polyhedra clipped by a paraboloid
 59 surface (as in [21, 22]). Moreover, we require this estimation to (a) reach machine
 60 accuracy, while (b) maintaining a computational expense that is low enough to enable
 61 its *on-the-fly* execution in typical numerical applications (e.g., the simulation of two-
 62 phase flows with finite-volumes), and (c) being robust to singular configurations (e.g.,
 63 paraboloid surfaces being parabolic cylinder or planes, and/or ambiguous discrete in-
 64 tersection topologies). These choices and requirements, although mainly motivated
 65 by the use of these moments for simulating two-phase flows, may also find applica-
 66 tions in the numerical fields listed above. A main difficulty in clipping a polyhedron
 67 with a paraboloid lies in the fact that the faces of the clipped polyhedron cannot sys-
 68 tematically be represented with non-rational or rational Bézier patches [27, 24]. This
 69 prevents the use of recently proposed integration strategies designed for curved poly-
 70 hedra bounded by Bézier or B-spline surfaces [7, 3]. By successive applications of the
 71 divergence theorem, we show that the first moments of the clipped polyhedron can be
 72 expressed as a sum of one-dimensional integrals over straight line segments and conic
 73 section arcs. With a parametrization of the latter into rational Bézier arcs, we derive
 74 closed-form expressions for the first moments, rendering their numerical estimation
 75 exact within machine accuracy. Implemented within the half-edge data structure of
 76 the open-source **Interface Reconstruction Library** [8]*, the computational cost
 77 of these moment estimations is kept within an order of magnitude of that of clipping
 78 a polyhedron with a half-space. Finally, our choice of arc parametrization, in con-
 79 junction with the detection and treatment of ambiguous discrete topologies, allows for
 80 robust moment estimates even in degenerate configurations.

81 The remainder of this manuscript is organized as follows: Section 2 introduces the
 82 problem that we address and the notations employed throughout the manuscript.
 83 The closed-form expressions of the clipped polyhedron’s first moments are derived in
 84 Section 3. Section 4 touches upon the integration of quantities (e.g., the moments) of

*The **Interface Reconstruction Library** (IRL) source code is available under Mozilla Public License 2.0 (MPL-2.0) at https://github.com/robert-chiodi/interface-reconstruction-library/tree/paraboloid_cutting.

85 the clipped polyhedron's curved face(s). [Section 5](#) details the procedure employed for
 86 preventing ambiguous clipped polyhedron topologies. [Section 6](#) discusses the exten-
 87 sion of our approach to higher-order moments. Finally, the accuracy, efficiency, and
 88 robustness of our proposed integration strategy are assessed in [Section 7](#), and we draw
 89 conclusions in [Section 8](#).

90 **2. Problem statement.** Consider the two following subsets of \mathbb{R}^3 :

- 91 • A polyhedron \mathcal{P} delimited by $n_{\mathcal{F}}$ planar polygonal faces $\mathcal{F}_i, i \in \{1, \dots, n_{\mathcal{F}}\}$,
 92 each equipped with an outward-pointing normal vector \mathbf{n}_i (e.g., see [Figures 1a](#)
 93 and [1b](#)). Neither \mathcal{P} nor its faces \mathcal{F}_i are required to be convex.

- 94 • The region \mathcal{Q} , located on one side of a paraboloid \mathcal{S} (e.g., see [Figure 1c](#)).

95 Without loss of generality, we assume to be working in a Cartesian coordinate system
 96 equipped with the orthonormal basis $(\mathbf{e}_x, \mathbf{e}_y, \mathbf{e}_z)$, within which the position vector
 97 reads $\mathbf{x} = [x \ y \ z]^T$, and where \mathcal{Q} and \mathcal{S} are implicitly defined as

98 (2.1)
$$\mathcal{Q} = \{\mathbf{x} \in \mathbb{R}^3 : \phi(\mathbf{x}) \leq 0\},$$

99 (2.2)
$$\mathcal{S} = \{\mathbf{x} \in \mathbb{R}^3 : \phi(\mathbf{x}) = 0\},$$

101 with

102 (2.3)
$$\phi : \begin{cases} \mathbb{R}^3 & \rightarrow \mathbb{R} \\ \mathbf{x} & \mapsto \alpha x^2 + \beta y^2 + z, \end{cases} \quad (\alpha, \beta) \in \mathbb{R}^2.$$

103 These assumptions do not restrict \mathcal{Q} and \mathcal{S} since, for any paraboloid-bounded clipping
 104 region in \mathbb{R}^3 , there exists a combination of rotations and translations of the canonical
 105 coordinate system resulting in such implicit definitions of \mathcal{Q} and \mathcal{S} . For the sake of
 106 clarity and conciseness, we introduce the following notations:

- 107 • The subscript \square_i refers to a topological element or quantity related to the
 108 i th face of the polyhedron \mathcal{P} .
- 109 • The superscript $\hat{\square}$ implies an intersection with the clipping region \mathcal{Q} , e.g.,
 110 $\hat{\mathcal{P}} \equiv \mathcal{P} \cap \mathcal{Q}$ or $\hat{\mathcal{F}}_i \equiv \mathcal{F}_i \cap \mathcal{Q}$.
- 111 • The superscript $\tilde{\square}$ implies an intersection with the polyhedron \mathcal{P} , e.g., $\tilde{\mathcal{S}} \equiv \mathcal{S} \cap \mathcal{P}$.
 112 This means that $\hat{\mathcal{P}} \equiv \tilde{\mathcal{Q}}$.

113 As mentioned in [Section 1](#), we are interested in calculating the zeroth and first mo-
 114 ments of $\hat{\mathcal{P}} = \mathcal{P} \cap \mathcal{Q}$ (e.g., see [Figure 1e](#)), i.e., its volume and volume-weighted cen-
 115 troid, given as

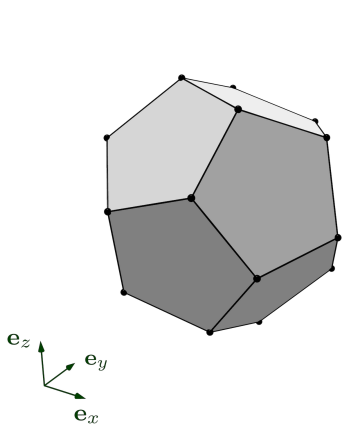
116 (2.4)
$$M_0^{\hat{\mathcal{P}}} = \int_{\hat{\mathcal{P}}} 1 \, d\mathbf{x}, \quad \text{and} \quad \mathbf{M}_1^{\hat{\mathcal{P}}} = \int_{\hat{\mathcal{P}}} \mathbf{x} \, d\mathbf{x}.$$

118 In the remainder of this work, we shall refer to these quantities as "the first moments"
 119 or "the moments" of $\hat{\mathcal{P}}$, which we group into the vector

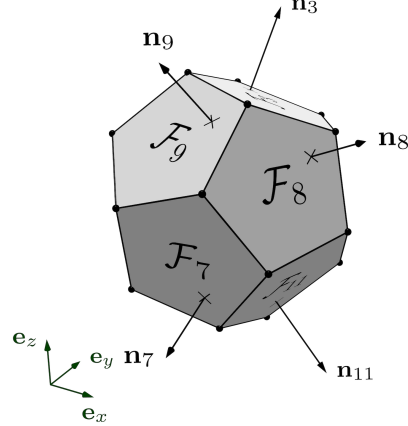
120 (2.5)
$$\mathbf{M}^{\hat{\mathcal{P}}} = \begin{bmatrix} M_0^{\hat{\mathcal{P}}} \\ \mathbf{M}_1^{\hat{\mathcal{P}}} \end{bmatrix} = \int_{\hat{\mathcal{P}}} \boldsymbol{\Upsilon}(\mathbf{x}) \, d\mathbf{x},$$

122 where

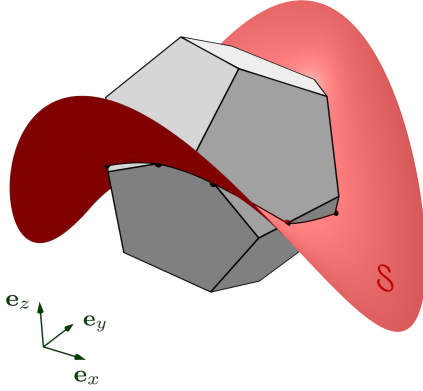
123 (2.6)
$$\boldsymbol{\Upsilon} : \begin{cases} \mathbb{R}^3 & \rightarrow \mathbb{R}^4 \\ \mathbf{x} & \mapsto [1 \ x \ y \ z]^T \end{cases}.$$



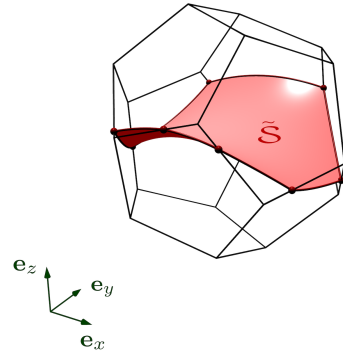
(a) A polyhedron $\mathcal{P} \subset \mathbb{R}^3$. In this example, \mathcal{P} is a regular dodecahedron with $n_{\mathcal{F}} = 12$ faces.



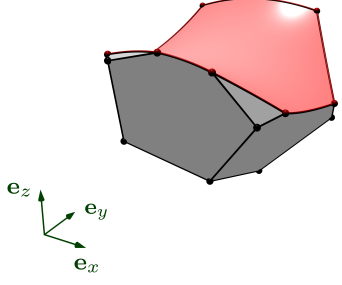
(b) The faces of $\partial\mathcal{P} = \cup_i \mathcal{F}_i$ and their outward-pointing normal vectors, \mathbf{n}_i , $i \in \{1, \dots, n_{\mathcal{F}}\}$.



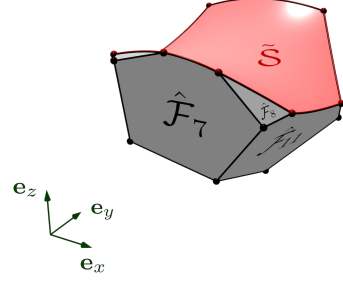
(c) A paraboloid surface \mathcal{S} intersecting \mathcal{P} . The domain \mathcal{Q} is the subset of \mathbb{R}^3 located below \mathcal{S} , with respect to \mathbf{e}_z .



(d) The intersection of the paraboloid \mathcal{S} with the polyhedron \mathcal{P} , $\tilde{\mathcal{S}} = \mathcal{S} \cap \mathcal{P}$.



(e) The clipped polyhedron $\hat{\mathcal{P}} = \mathcal{P} \cap \mathcal{Q}$, where \mathcal{Q} is the subset of \mathbb{R}^3 below \mathcal{S} .



(f) The faces of $\partial\hat{\mathcal{P}} = \cup_i \hat{\mathcal{F}}_i \cup \tilde{\mathcal{S}}$.

FIG. 1. A polyhedron $\mathcal{P} \subset \mathbb{R}^3$ intersected by the clipping region $\mathcal{Q} \subset \mathbb{R}^3$ located below a paraboloid surface \mathcal{S} .

124 **3. Moments derivation.** Using the divergence theorem, Eq. (2.5) can be rewritten as

$$126 \quad (3.1) \quad \mathbf{M}^{\hat{\mathcal{P}}} = \int_{\hat{\mathcal{P}}} \nabla \cdot (\Phi(\mathbf{x}) \otimes \mathbf{e}_z) \, d\mathbf{x} = \int_{\partial\hat{\mathcal{P}}} \Phi(\mathbf{x})(\mathbf{n}_{\partial\hat{\mathcal{P}}} \cdot \mathbf{e}_z) \, d\mathbf{a},$$

127 where $d\mathbf{a}$ is an infinitesimal surface element on $\partial\hat{\mathcal{P}} = \cup_i \hat{\mathcal{F}}_i \cup \tilde{\mathcal{S}}$, the boundary of $\hat{\mathcal{P}}$,
128 $\mathbf{n}_{\partial\hat{\mathcal{P}}}$ is the normal to $\partial\hat{\mathcal{P}}$ pointing towards the outside of $\hat{\mathcal{P}}$, and Φ is defined as

$$129 \quad (3.2) \quad \Phi : \begin{cases} \mathbb{R}^3 & \rightarrow \mathbb{R}^4 \\ \mathbf{x} & \mapsto \int_0^z \boldsymbol{\Upsilon}(\mathbf{x}) \, dz \quad (= [z \quad xz \quad yz \quad \frac{1}{2}z^2]^T) \end{cases} .$$

130 Eq. (3.1) can be split into the following sum of integrals,

$$131 \quad (3.3) \quad \mathbf{M}^{\hat{\mathcal{P}}} = \int_{\tilde{\mathcal{S}}} \Phi(\mathbf{x})(\mathbf{n}_{\tilde{\mathcal{S}}} \cdot \mathbf{e}_z) \, d\mathbf{a} + \sum_{i=1}^{n_{\mathcal{F}}} \int_{\hat{\mathcal{F}}_i} \Phi(\mathbf{x})(\mathbf{n}_i \cdot \mathbf{e}_z) \, d\mathbf{a},$$

132 where $\tilde{\mathcal{S}} = \mathcal{S} \cap \mathcal{P}$ is the portion of the paraboloid \mathcal{S} inside the polyhedron \mathcal{P} (e.g.,
133 see Figure 1d), $\mathbf{n}_{\tilde{\mathcal{S}}}$ is the normal to $\tilde{\mathcal{S}}$ pointing outwards of \mathcal{Q} (i.e., $\mathbf{n}_{\tilde{\mathcal{S}}} \cdot \mathbf{e}_z \geq 0$),
134 and $\hat{\mathcal{F}}_i = \mathcal{F}_i \cap \mathcal{Q}$ is the portion of the face \mathcal{F}_i inside the clipping region \mathcal{Q} (e.g., see
135 Figure 1f). Owing to the definitions of \mathcal{Q} and \mathcal{S} , as given in Eqs. (2.1) and (2.2), the
136 normal to \mathcal{S} pointing outwards of \mathcal{Q} reads as

$$137 \quad (3.4) \quad \mathbf{n}_{\mathcal{S}} = \frac{\nabla\phi}{\|\nabla\phi\|},$$

138 yielding

$$139 \quad (3.5) \quad \mathbf{M}^{\hat{\mathcal{P}}} = \int_{\tilde{\mathcal{S}}} \Phi(\mathbf{x}) \left(\frac{\nabla\phi(\mathbf{x}) \cdot \mathbf{e}_z}{\|\nabla\phi(\mathbf{x})\|} \right) \, d\mathbf{a} + \sum_{i=1}^{n_{\mathcal{F}}} \int_{\hat{\mathcal{F}}_i} \Phi(\mathbf{x})(\mathbf{n}_i \cdot \mathbf{e}_z) \, d\mathbf{a}.$$

140 The surface $\tilde{\mathcal{S}}$ can be expressed in the parametric form

$$141 \quad (3.6) \quad \tilde{\mathcal{S}} = \left\{ \begin{bmatrix} x \\ y \\ -\alpha x^2 - \beta y^2 \end{bmatrix}, (x, y) \in \tilde{\mathcal{S}}^\perp \right\},$$

142 with α and β the coefficients introduced in Eq. (2.3), and with $\tilde{\mathcal{S}}^\perp$ the projection of $\tilde{\mathcal{S}}$ onto the xy -plane. Under the assumption that $\mathbf{n}_i \cdot \mathbf{e}_z \neq 0$, each face $\hat{\mathcal{F}}_i$,
143 $i \in \{1, \dots, n_{\mathcal{F}}\}$, can also be expressed in the parametric form

$$145 \quad (3.7) \quad \hat{\mathcal{F}}_i = \left\{ \begin{bmatrix} x \\ y \\ \delta_i - \lambda_i x - \tau_i y \end{bmatrix}, (x, y) \in \hat{\mathcal{F}}_i^\perp \right\},$$

146 with

$$147 \quad (3.8) \quad \delta_i = \frac{\mathbf{n}_i \cdot \mathbf{x}_{\mathcal{F}_i}}{\mathbf{n}_i \cdot \mathbf{e}_z}, \quad \text{for any } \mathbf{x}_{\mathcal{F}_i} \in \mathcal{F}_i,$$

$$148 \quad (3.9) \quad \lambda_i = \frac{\mathbf{n}_i \cdot \mathbf{e}_x}{\mathbf{n}_i \cdot \mathbf{e}_z},$$

$$149 \quad (3.10) \quad \tau_i = \frac{\mathbf{n}_i \cdot \mathbf{e}_y}{\mathbf{n}_i \cdot \mathbf{e}_z},$$

151 and with $\hat{\mathcal{F}}_i^\perp$ the projection of $\hat{\mathcal{F}}_i$ onto the xy -plane. These explicit parametrizations
 152 yield

$$153 \quad (3.11) \quad \mathcal{M}^{\hat{\mathcal{P}}} = \int_{\tilde{\mathcal{S}}^\perp} \Phi_S(x, y) \, d\mathbf{a}^\perp + \sum_{i=1}^{n_{\mathcal{F}}} \text{sign}(\mathbf{n}_i \cdot \mathbf{e}_z) \int_{\hat{\mathcal{F}}_i^\perp} \Phi_{\mathcal{F}_i}(x, y) \, d\mathbf{a}^\perp,$$

154 where Φ_S and $\Phi_{\mathcal{F}_i}$ are the function vectors

$$155 \quad (3.12) \quad \Phi_S(x, y) = \begin{bmatrix} -\alpha x^2 - \beta y^2 \\ -\alpha x^3 - \beta x y^2 \\ -\alpha y x^2 - \beta y^3 \\ \frac{1}{2} (\alpha x^2 + \beta y^2)^2 \end{bmatrix}, \quad \Phi_{\mathcal{F}_i}(x, y) = \begin{bmatrix} \delta_i - \lambda_i x - \tau_i y \\ \delta_i x - \lambda_i x^2 - \tau_i x y \\ \delta_i y - \lambda_i x y - \tau_i y^2 \\ \frac{1}{2} (\delta_i - \lambda_i x - \tau_i y)^2 \end{bmatrix},$$

156 and $d\mathbf{a}^\perp = dx dy$ is an infinitesimal surface element on the xy -plane. Note that in
 157 order to simplify Eq. (3.5) into (3.11), we have used the fact that $\|\nabla\phi(\mathbf{x})\|$ is the
 158 determinant of the parametrization (3.6) of $\tilde{\mathcal{S}}$, and that $|\mathbf{n}_i \cdot \mathbf{e}_z|^{-1}$ is the determinant
 159 of the parametrization (3.7) of $\hat{\mathcal{F}}_i$. The projected integration domains $\tilde{\mathcal{S}}^\perp$ and $\hat{\mathcal{F}}_i^\perp$
 160 corresponding to the configuration of Figure 1 are illustrated in Figure 2.

161 Eq. (3.11) can be rewritten as

$$162 \quad (3.13) \quad \mathcal{M}^{\hat{\mathcal{P}}} = \int_{\tilde{\mathcal{S}}^\perp} \nabla \cdot (\Psi_S(x, y) \otimes \mathbf{e}_x) \, d\mathbf{a}^\perp + \sum_{i=1}^{n_{\mathcal{F}}} \text{sign}(\mathbf{n}_i \cdot \mathbf{e}_z) \int_{\hat{\mathcal{F}}_i^\perp} \nabla \cdot (\Psi_{\mathcal{F}_i}(x, y) \otimes \mathbf{e}_x) \, d\mathbf{a}^\perp,$$

165 where Ψ_S and $\Psi_{\mathcal{F}_i}$ are defined as

$$166 \quad (3.14) \quad \Psi_S : \begin{cases} \mathbb{R}^2 & \rightarrow \mathbb{R}^4 \\ (x, y) & \mapsto \int_0^x \Phi_S(x, y) \, dx \end{cases}.$$

167 and $\forall i \in \{1, \dots, n_{\mathcal{F}}\}$,

$$168 \quad (3.15) \quad \Psi_{\mathcal{F}_i} : \begin{cases} \mathbb{R}^2 & \rightarrow \mathbb{R}^4 \\ (x, y) & \mapsto \int_0^x \Phi_{\mathcal{F}_i}(x, y) \, dx \end{cases}.$$

169 Note that the choice made here of integrating Φ_S and $\Phi_{\mathcal{F}_i}$ with respect to x is arbi-
 170 trary, and that we could have equivalently integrated them with respect to y , requiring
 171 to replace \mathbf{e}_x by \mathbf{e}_y in Eq. (3.13). Using the divergence theorem once again, this gives

$$172 \quad (3.16) \quad \mathcal{M}^{\hat{\mathcal{P}}} = \int_{\partial\tilde{\mathcal{S}}^\perp} \Psi_S(x, y) (\mathbf{n}_{\partial\tilde{\mathcal{S}}^\perp} \cdot \mathbf{e}_x) \, dl + \sum_{i=1}^{n_{\mathcal{F}}} \int_{\partial\hat{\mathcal{F}}_i^\perp} \Psi_{\mathcal{F}_i}(x, y) (\mathbf{n}_{\partial\hat{\mathcal{F}}_i^\perp} \cdot \mathbf{e}_x) \, dl,$$

173 where dl is an infinitesimal line element on the integration domains $\partial\tilde{\mathcal{S}}^\perp$ and $\partial\hat{\mathcal{F}}_i^\perp$,
 174 which are the boundaries of the projections of the faces of $\hat{\mathcal{P}}$ onto the xy -plane.
 175 As such, they consist of closed curves in the xy -plane, that are successions of conic
 176 section arcs and/or line segments (e.g., see Figures 2b and 2c). Note that the term
 177 “ $\text{sign}(\mathbf{n}_i \cdot \mathbf{e}_z)$ ” is now implicitly accounted for, as the closed curves $\partial\hat{\mathcal{F}}_i$ (and therefore
 178 their projection onto the xy -plane, $\partial\hat{\mathcal{F}}_i^\perp$) are oriented so as to produce a normal
 179 vector pointing towards the outside of $\hat{\mathcal{P}}$. It should also be noted that the integration

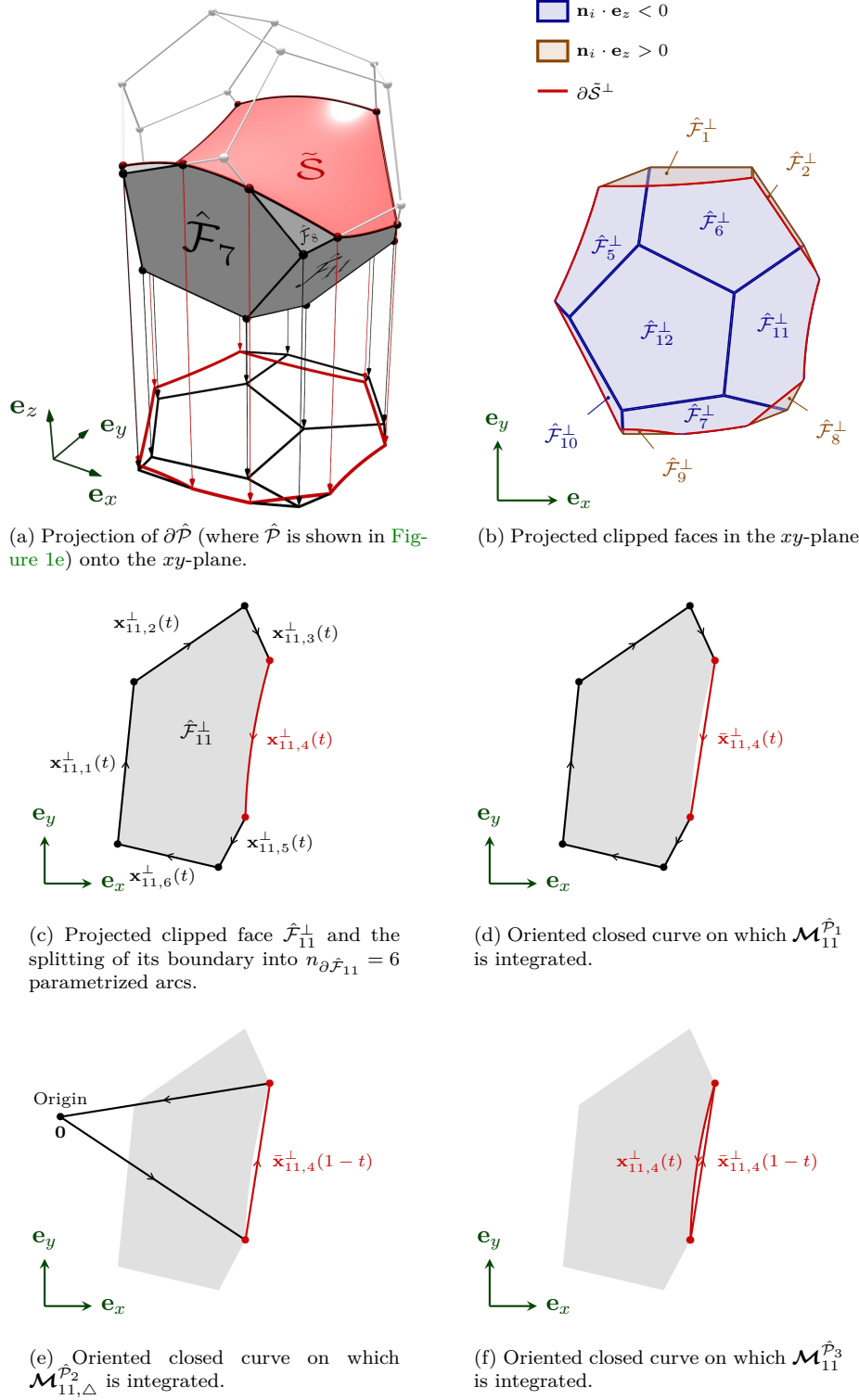


FIG. 2. Illustration of the one-dimensional integration domains used for integrating the first, second, and third contributions to the moments.

180 domains $\partial\tilde{\mathcal{S}}^\perp$ and $\partial\hat{\mathcal{F}}_i^\perp$ do not necessarily consist of one closed curve each – they may
 181 each be the union of several non-intersecting oriented closed curves.

182 Let us assume that a parametrization

183 (3.17) $\mathbf{x}_{i,j}(t) = x_{i,j}(t)\mathbf{e}_x + y_{i,j}(t)\mathbf{e}_y + z_{i,j}(t)\mathbf{e}_z, \quad t \in [0, 1], \quad j \in \{1, \dots, n_{\partial\hat{\mathcal{F}}_i}\},$

184 is known for each of the $n_{\partial\hat{\mathcal{F}}_i}$ arcs of $\partial\hat{\mathcal{F}}_i$, where the functions $x_{i,j}$, $y_{i,j}$, and $z_{i,j}$ belong
 185 to $C^1([0, 1])$. Moreover, let us note that each parametrized conic section arc belonging
 186 to $\partial\tilde{\mathcal{S}}$ is necessarily present in one and only one of the clipped face boundaries $\partial\hat{\mathcal{F}}_i$,
 187 where it is traversed in the opposite direction for integrating $\Psi_{\mathcal{F}_i}$. Eq. (3.16) can then
 188 be written as

189 (3.18) $\mathcal{M}^{\hat{\mathcal{P}}} = \sum_{i=1}^{n_{\mathcal{F}}} \sum_{j=1}^{n_{\partial\hat{\mathcal{F}}_i}} \int_0^1 \left(\Psi_{\mathcal{F}_i}(x_{i,j}(t), y_{i,j}(t)) - 1_{i,j}^{\partial\tilde{\mathcal{S}}} \Psi_{\mathcal{S}}(x_{i,j}(t), y_{i,j}(t)) \right) y'_{i,j}(t) dt,$
 190

191 where

192 (3.19) $1_{i,j}^{\partial\tilde{\mathcal{S}}} = \begin{cases} 1 & \text{if the } j\text{th arc of } \partial\hat{\mathcal{F}}_i \text{ also belongs to } \partial\tilde{\mathcal{S}} \\ 0 & \text{otherwise} \end{cases}.$
 193

194 Note that in Eq. (3.18) and in the remainder of this manuscript, the superscript \square'
 195 indicates that a function has been differentiated with respect to its unique variable.
 196 A closed-form expression can be derived for the integral in Eq. (3.18), however, its
 197 use for numerically calculating the moments is undesirable for two main reasons:

- 198 1. the expression contains many terms, rendering its numerical calculation ex-
 199 pensive;
 200 2. the expression depends on δ_i , λ_i , and τ_i , which all tend towards infinity as
 201 $\mathbf{n}_i \cdot \mathbf{e}_z$ tends towards zero, leading to large round-off errors in the context of
 202 floating-point arithmetics.

203 Instead, the introduction of a twin parametrization of the arcs of $\partial\hat{\mathcal{P}}$ and the ju-
 204 dicious splitting of the integral in Eq. (3.18) can both reduce the complexity of its
 205 closed-form expression and remove its direct dependency on the potentially singular
 206 coefficients δ_i , λ_i , and τ_i . Let us then introduce the parametrization

207 (3.20) $\bar{\mathbf{x}}_{i,j}(t) = \bar{x}_{i,j}(t)\mathbf{e}_x + \bar{y}_{i,j}(t)\mathbf{e}_y + \bar{z}_{i,j}(t)\mathbf{e}_z, \quad t \in [0, 1], \quad j \in \{1, \dots, n_{\partial\hat{\mathcal{F}}_i}\},$

208 which links $\mathbf{x}_{i,j}(0)$ to $\mathbf{x}_{i,j}(1)$ by a straight line. For the sake of conciseness, we shall
 209 refer to these two points as $\mathbf{x}_{i,j}(0) = \mathbf{x}_{i,j,0}$ and $\mathbf{x}_{i,j}(1) = \mathbf{x}_{i,j,1}$ in the remainder of this
 210 work. This twin parametrization of each arc is simply given as

211 (3.21) $\bar{\mathbf{x}}_{i,j}(t) = (1-t)\mathbf{x}_{i,j,0} + t\mathbf{x}_{i,j,1}, \quad t \in [0, 1], \quad j \in \{1, \dots, n_{\partial\hat{\mathcal{F}}_i}\}.$

212 If the j th arc of $\partial\hat{\mathcal{F}}_i$ does not belong to $\tilde{\mathcal{S}}$, then $x_{i,j} \equiv \bar{x}_{i,j}$, $y_{i,j} \equiv \bar{y}_{i,j}$ and $z_{i,j} \equiv \bar{z}_{i,j}$.

213 We can then re-organize Eq. (3.18) as

$$(3.22)$$

$$\begin{aligned} 214 \quad \mathcal{M}^{\hat{\mathcal{P}}} &= \sum_{i=1}^{n_{\mathcal{F}}} \sum_{j=1}^{n_{\partial\hat{\mathcal{F}}_i}} \left[\int_0^1 \Psi_{\mathcal{F}_i}(\bar{x}_{i,j}(t), \bar{y}_{i,j}(t)) \bar{y}'_{i,j}(t) dt \right. \\ 215 \quad &\quad - 1_{i,j}^{\partial\tilde{\mathcal{S}}} \int_0^1 \Psi_{\mathcal{S}}(\bar{x}_{i,j}(t), \bar{y}_{i,j}(t)) \bar{y}'_{i,j}(t) dt \\ 216 \quad &\quad - 1_{i,j}^{\partial\tilde{\mathcal{S}}} \int_0^1 \left(\Psi_{\mathcal{F}_i}(\bar{x}_{i,j}(t), \bar{y}_{i,j}(t)) - \Psi_{\mathcal{S}}(\bar{x}_{i,j}(t), \bar{y}_{i,j}(t)) \right) \bar{y}'_{i,j}(t) \\ 217 \quad &\quad \left. + \left(\Psi_{\mathcal{S}}(x_{i,j}(t), y_{i,j}(t)) - \Psi_{\mathcal{F}_i}(x_{i,j}(t), y_{i,j}(t)) \right) y'_{i,j}(t) dt \right], \\ 218 \end{aligned}$$

219 The moments can thus be described as the sum of three distinct contributions, i.e.,

$$220 \quad (3.23) \quad \mathcal{M}^{\hat{\mathcal{P}}} = \mathcal{M}^{\hat{\mathcal{P}}_1} + \mathcal{M}^{\hat{\mathcal{P}}_2} + \mathcal{M}^{\hat{\mathcal{P}}_3} = \sum_{i=1}^{n_{\mathcal{F}}} \mathcal{M}_i^{\hat{\mathcal{P}}_1} + \sum_{i=1}^{n_{\mathcal{F}}} \mathcal{M}_i^{\hat{\mathcal{P}}_2} + \sum_{i=1}^{n_{\mathcal{F}}} \mathcal{M}_i^{\hat{\mathcal{P}}_3},$$

221 where

$$222 \quad (3.24) \quad \mathcal{M}_i^{\hat{\mathcal{P}}_1} = \int_0^1 \sum_{j=1}^{n_{\partial\hat{\mathcal{F}}_i}} \Psi_{\mathcal{F}_i}(\bar{x}_{i,j}(t), \bar{y}_{i,j}(t)) \bar{y}'_{i,j}(t) dt,$$

$$223 \quad (3.25) \quad \mathcal{M}_i^{\hat{\mathcal{P}}_2} = \int_0^1 \sum_{j=1}^{n_{\partial\hat{\mathcal{F}}_i}} -1_{i,j}^{\partial\tilde{\mathcal{S}}} \Psi_{\mathcal{S}}(\bar{x}_{i,j}(t), \bar{y}_{i,j}(t)) \bar{y}'_{i,j}(t) dt,$$

$$224 \quad (3.26) \quad \mathcal{M}_i^{\hat{\mathcal{P}}_3} = \int_0^1 \sum_{j=1}^{n_{\partial\hat{\mathcal{F}}_i}} 1_{i,j}^{\partial\tilde{\mathcal{S}}} \left((\Psi_{\mathcal{S}}(\bar{x}_{i,j}(t), \bar{y}_{i,j}(t)) - \Psi_{\mathcal{F}_i}(\bar{x}_{i,j}(t), \bar{y}_{i,j}(t))) \bar{y}'_{i,j}(t) \right. \\ 225 \quad \left. + (\Psi_{\mathcal{F}_i}(x_{i,j}(t), y_{i,j}(t)) - \Psi_{\mathcal{S}}(x_{i,j}(t), y_{i,j}(t))) y'_{i,j}(t) \right) dt.$$

227 The contributions $\mathcal{M}^{\hat{\mathcal{P}}_1}$ and $\mathcal{M}^{\hat{\mathcal{P}}_2}$ require the integration of the paraboloid and plane
228 primitives over straight lines only (e.g., see Figures 2d and 2e), hence are straight-
229 forward to derive. The contribution $\mathcal{M}^{\hat{\mathcal{P}}_3}$, on the other hand, requires the paramet-
230 rization of the conic section arcs in $\partial\tilde{\mathcal{S}}$ (e.g., see Figure 2f). It should also be noted
231 that each arc of the clipped faces $\partial\hat{\mathcal{F}}_i$ contributes to $\mathcal{M}^{\hat{\mathcal{P}}_1}$, whereas only the conic
232 section arcs in those faces (originating from the intersection of $\partial\mathcal{P}$ with \mathcal{S}) contribute
233 to $\mathcal{M}^{\hat{\mathcal{P}}_2}$ and $\mathcal{M}^{\hat{\mathcal{P}}_3}$, owing to the presence of the coefficient $1_{i,j}^{\partial\tilde{\mathcal{S}}}$.

234 **3.1. First term: $\mathcal{M}^{\hat{\mathcal{P}}_1}$.** Let us be reminded that the boundary of each clipped
235 face, $\partial\hat{\mathcal{F}}_i$, is a succession of $n_{\partial\hat{\mathcal{F}}_i}$ conic section arcs and/or straight line segments that
236 each link a start point $\mathbf{x}_{i,j,0}$ to an end point $\mathbf{x}_{i,j,1}$. Now recall that we aim to derive
237 expressions that are free of the coefficients δ_i , λ_i , and τ_i , so as to avoid round-off errors
238 in the numerical calculation of the moments. To do so, we assign to each face $\hat{\mathcal{F}}_i$ a
239 reference point $\mathbf{x}_{i,\text{ref}}$ whose only requirement is to belong to the plane containing $\hat{\mathcal{F}}_i$,
240 e.g., $\mathbf{x}_{i,\text{ref}} = \mathbf{x}_{i,1,0}$. For each arc of each clipped face, rather than integrating on
241 the straight line linking $\mathbf{x}_{i,j,0}$ to $\mathbf{x}_{i,j,1}$, we integrate instead on the oriented triangle
242 $T_{i,j}^{(1)} = (\mathbf{x}_{i,j,0}, \mathbf{x}_{i,j,1}, \mathbf{x}_{i,\text{ref}})$. Since $\partial\hat{\mathcal{F}}_i$ is the union of closed curves, the start point of
243 each of its constituting arcs is necessarily the end point of another arc, and the sum

244 of all these triangle integrals is equal to the sum of the straight arc integrals. In other
 245 terms, substituting Eq. (3.21) into Eq. (3.24), the latter can be rewritten as

(3.27)

$$\begin{aligned} 246 \quad \mathcal{M}_i^{\hat{\mathcal{P}}_1} &= \int_0^1 \sum_{j=1}^{n_{\partial\hat{\mathcal{F}}_i}} \Psi_{\mathcal{F}_i}((1-t)x_{i,j,0} + tx_{i,j,1}, (1-t)y_{i,j,0} + ty_{i,j,1})(y_{i,j,1} - y_{i,j,0}) dt, \\ 247 \quad &= \int_0^1 \sum_{j=1}^{n_{\partial\hat{\mathcal{F}}_i}} \left(\begin{array}{l} \Psi_{\mathcal{F}_i}((1-t)x_{i,j,0} + tx_{i,j,1}, (1-t)y_{i,j,0} + ty_{i,j,1})(y_{i,j,1} - y_{i,j,0}) \\ + \Psi_{\mathcal{F}_i}((1-t)x_{i,j,1} + tx_{i,\text{ref}}, (1-t)y_{i,j,1} + ty_{i,\text{ref}})(y_{i,\text{ref}} - y_{i,j,1}) \\ + \Psi_{\mathcal{F}_i}((1-t)x_{i,\text{ref}} + tx_{i,j,0}, (1-t)y_{i,\text{ref}} + ty_{i,j,0})(y_{i,j,0} - y_{i,\text{ref}}) \end{array} \right) dt. \\ 248 \end{aligned}$$

249 Making use of Eqs. (3.12) and (3.15), and of the fact that

$$250 \quad z_{i,\text{ref}} = \delta_i - \lambda_i x_{i,\text{ref}} - \tau_i y_{i,\text{ref}}$$

$$251 \quad z_{i,j} = \delta_i - \lambda_i x_{i,j} - \tau_i y_{i,j}, \quad \forall j \in \{1, \dots, n_{\partial\hat{\mathcal{F}}_i}\}$$

253 it follows that

$$254 \quad (3.30) \quad \mathcal{M}_i^{\hat{\mathcal{P}}_1} = \sum_{j=1}^{n_{\partial\hat{\mathcal{F}}_i}} \mathcal{A}(\mathbf{x}_{i,j,0}, \mathbf{x}_{i,j,1}, \mathbf{x}_{i,\text{ref}}) \mathcal{B}^{(1)}(\mathbf{x}_{i,j,0}, \mathbf{x}_{i,j,1}, \mathbf{x}_{i,\text{ref}}),$$

255 where \mathcal{A} is the operator for calculating the signed projected area of a triangle from
 256 the knowledge of its three corners, i.e.,

$$258 \quad (3.31) \quad \mathcal{A} : \begin{cases} \mathbb{R}^3 \times \mathbb{R}^3 \times \mathbb{R}^3 & \rightarrow \mathbb{R} \\ (\mathbf{x}_a, \mathbf{x}_b, \mathbf{x}_c) & \mapsto \frac{1}{2}(x_a(y_b - y_c) + x_b(y_c - y_a) + x_c(y_a - y_b)) \end{cases},$$

259 and $\mathcal{B}^{(1)} : \mathbb{R}^3 \times \mathbb{R}^3 \times \mathbb{R}^3 \rightarrow \mathbb{R}^4$ reads as

$$260 \quad (3.32) \quad \mathcal{B}^{(1)}(\mathbf{x}_a, \mathbf{x}_b, \mathbf{x}_c) = \frac{1}{12} \begin{bmatrix} 4(z_a + z_b + z_c) \\ (z_a + z_b + z_c)(x_a + x_b + x_c) + x_a z_a + x_b z_b + x_c z_c \\ (z_a + z_b + z_c)(y_a + y_b + y_c) + y_a z_a + y_b z_b + y_c z_c \\ z_a^2 + z_b^2 + z_c^2 + z_b z_c + z_a z_b + z_a z_c \end{bmatrix}.$$

261 **3.2. Second term:** $\mathcal{M}_i^{\hat{\mathcal{P}}_2}$. For computing $\mathcal{M}_i^{\hat{\mathcal{P}}_2}$, similarly as in Subsection 3.1,
 262 we choose a reference point \mathbf{x}_S belonging to \mathcal{S} . An obvious choice for this reference
 263 point is the origin of our coordinate system, i.e., $\mathbf{x}_S = \mathbf{0}$. For each conic section arc
 264 of each clipped face, rather than integrating on the straight line linking $\mathbf{x}_{i,j,0}$ to $\mathbf{x}_{i,j,1}$,
 265 we integrate instead on the oriented triangle $T_{i,j}^{(2)} = (\mathbf{x}_{i,j,0}, \mathbf{x}_{i,j,1}, \mathbf{x}_S)$. For each i th
 266 face of \mathcal{P} , this yields the moment contribution

(3.33)

$$267 \quad \mathcal{M}_{i,\Delta}^{\hat{\mathcal{P}}_2} = \int_0^1 \sum_{j=1}^{n_{\partial\hat{\mathcal{F}}_i}} -1_{i,j}^{\partial\tilde{\mathcal{S}}} \left(\begin{array}{l} \Psi_S((1-t)x_{i,j,0} + tx_{i,j,1}, (1-t)y_{i,j,0} + ty_{i,j,1})(y_{i,j,1} - y_{i,j,0}) \\ + \Psi_S((1-t)x_{i,j,1} + tx_S, (1-t)y_{i,j,1} + ty_S)(y_S - y_{i,j,1}) \\ + \Psi_S((1-t)x_S + tx_{i,j,0}, (1-t)y_S + ty_{i,j,0})(y_{i,j,0} - y_S) \end{array} \right) dt,$$

268 Using Eqs. (3.12) and (3.14), substituting $\mathbf{x}_S = \mathbf{0}$, and making use of the fact that

$$269 \quad (3.34) \quad 1_{i,j}^{\partial\tilde{\mathcal{S}}} \neq 0 \Leftrightarrow \begin{cases} z_{i,j,0} = -\alpha x_{i,j,0}^2 - \beta y_{i,j,0}^2 \\ z_{i,j,1} = -\alpha x_{i,j,1}^2 - \beta y_{i,j,1}^2 \end{cases}, \quad \forall j \in \{1, \dots, n_{\partial\hat{\mathcal{F}}_i}\}$$

272 it follows that

$$273 \quad (3.35) \quad \mathcal{M}_{i,\Delta}^{\hat{\mathcal{P}}_2} = \sum_{j=1}^{n_{\partial\hat{\mathcal{F}}_i}} 1_{i,j}^{\partial\tilde{\mathcal{S}}} \mathcal{A}(\mathbf{x}_{i,j,0}, \mathbf{x}_{i,j,1}, \mathbf{0}) \mathcal{B}^{(2)}(\mathbf{x}_{i,j,0}, \mathbf{x}_{i,j,1}),$$

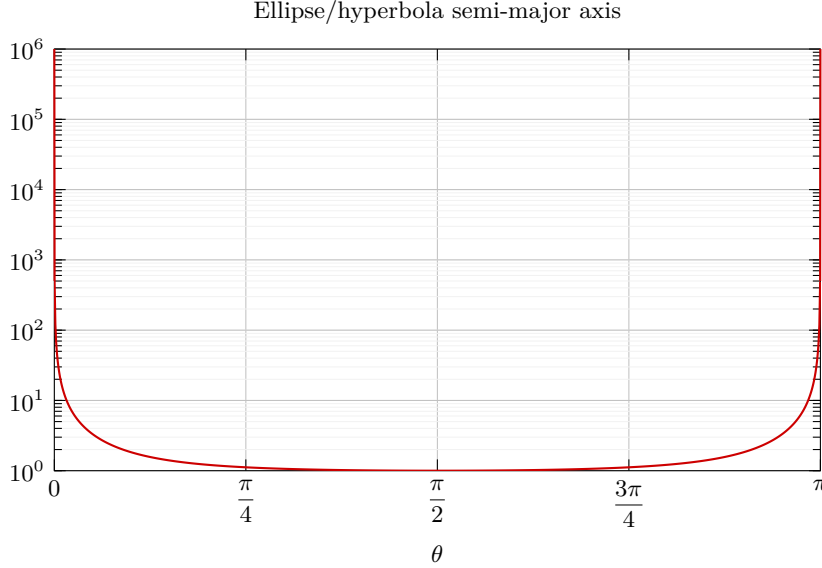


FIG. 3. Semi-major axis of the conic section generated by the intersection of the paraboloid \mathcal{S} , as defined in Eq. (2.2), when $\alpha = |\beta| = 1$, with the plane implicitly defined by $\mathbf{n} \cdot \mathbf{x} = -\mathbf{n} \cdot \mathbf{e}_z$, with $\mathbf{n} = [\cos(\theta) \ 0 \ \sin(\theta)]^\top$, as a function of the angle θ . The semi-major axis of the conic section tends to infinity when θ approaches a multiple of π , meaning that a parametrization of any arc of this conic section with trigonometric functions becomes singular if $\mathbf{n} \cdot \mathbf{e}_z \rightarrow 0$.

275 where \mathcal{A} is the signed projected triangle area operator defined in Eq. (3.31) and the
 276 operator $\mathcal{B}^{(2)} : \mathbb{R}^3 \times \mathbb{R}^3 \rightarrow \mathbb{R}^4$ reads as
 (3.36)

$$277 \quad \mathcal{B}^{(2)}(\mathbf{x}_a, \mathbf{x}_b) = \frac{1}{90} \begin{bmatrix} 15(\alpha x_a x_b + \beta y_a y_b - z_a - z_b) \\ 6\beta(y_a - y_b)(x_b y_a - x_a y_b) + 9(x_a + x_b)(z_a + z_b) \\ 6\alpha(x_a - x_b)(y_b x_a - y_a x_b) + 9(y_a + y_b)(z_a + z_b) \\ 2\alpha\beta(x_b y_a - x_a y_b)^2 + 3(z_a + z_b)(\alpha x_a x_b + \beta y_a y_b - z_a - z_b) + 3z_a z_b \end{bmatrix}.$$

278 Note that $\mathcal{M}_{i,\Delta}^{\hat{\mathcal{P}}_2} \neq \mathcal{M}_i^{\hat{\mathcal{P}}_2}$, owing to our choice of integrating over triangles rather than
 279 the individual arcs, however their sum over all faces is equal, yielding

$$280 \quad (3.37) \quad \mathcal{M}^{\hat{\mathcal{P}}_2} = \sum_{i=1}^{n_F} \mathcal{M}_{i,\Delta}^{\hat{\mathcal{P}}_2}.$$

281 **3.3. Third term:** $\mathcal{M}^{\hat{\mathcal{P}}_3}$. To derive a closed-form expression for $\mathcal{M}^{\hat{\mathcal{P}}_3}$, a pa-
 282 rametrization of the conic section arcs in $\partial\tilde{\mathcal{S}}$ must be provided. For the elliptic and
 283 hyperbolic cases, traditional parametrizations using trigonometric functions are obvi-
 284 ous choices, however they can yield significant round-off errors due to very large values
 285 of their constitutive parameters (e.g., the semi-major and semi-minor axes). This is
 286 illustrated in Figure 3 where the semi-major axis of the conic section generated by
 287 the intersection of a paraboloid with a plane is plotted as this plane is rotated about
 288 the \mathbf{e}_y basis vector. To avoid singular arc parametrizations, we express each conic
 289 section arc as a rational Bézier curve [15]. This provides a general parametrization
 290 that is valid over all conic section cases (i.e., elliptic, hyperbolic, and parabolic) and
 291 allows a seamless and smooth transition between cases. A conic section arc linking

292 a start point $\mathbf{x}_{i,j,0}$ to an end point $\mathbf{x}_{i,j,1}$ can be exactly represented by the rational
 293 quadratic Bézier curve parametrically defined as

$$294 \quad (3.38) \quad \mathbf{x}_{i,j}(t) = \frac{B_0(t)\mathbf{x}_{i,j,0} + w_{i,j}B_1(t)\mathbf{x}_{i,j}^* + B_2(t)\mathbf{x}_{i,j,1}}{B_0(t) + w_{i,j}B_1(t) + B_2(t)}, \quad t \in [0, 1],$$

295 where

$$296 \quad (3.39) \quad B_0(t) = (1-t)^2,$$

$$297 \quad (3.40) \quad B_1(t) = 2(1-t)t,$$

$$298 \quad (3.41) \quad B_2(t) = t^2,$$

300 are the Bernstein polynomials of degree 2, and $w_{i,j}$ is a weight associated with the
 301 control point $\mathbf{x}_{i,j}^*$. This control point is located at the intersection of the tangents to
 302 the conic section at the start and end points. In the case of the intersection of a planar
 303 face \mathcal{F}_i with a paraboloid surface \mathcal{S} , these tangents are obtained by the intersection
 304 of the planes tangent to \mathcal{S} at the start and end points, with the plane containing \mathcal{F}_i .
 305 The point $\mathbf{x}_{i,j}(\frac{1}{2})$ is, by definition, located at the intersection of \mathcal{S} with the segment
 306 linking $\bar{\mathbf{x}}_{i,j}(\frac{1}{2})$ to $\mathbf{x}_{i,j}^*$. Substituting t by $\frac{1}{2}$ in Eq. (3.38), it follows that

$$307 \quad (3.42) \quad w_{i,j}(\mathbf{x}_{i,j}(\frac{1}{2}) - \mathbf{x}_{i,j}^*) = \bar{\mathbf{x}}_{i,j}(\frac{1}{2}) - \mathbf{x}_{i,j}(\frac{1}{2}),$$

308 from which $w_{i,j}$ can be deducted. If $|w_{i,j}| < 1$, the rational Bézier curve is an arc
 309 of an ellipse, if $|w_{i,j}| = 1$, the rational Bézier curve is an arc of a parabola, and if
 310 $|w_{i,j}| > 1$, the rational Bézier curve is an arc of a hyperbola (e.g., see Figure 4).

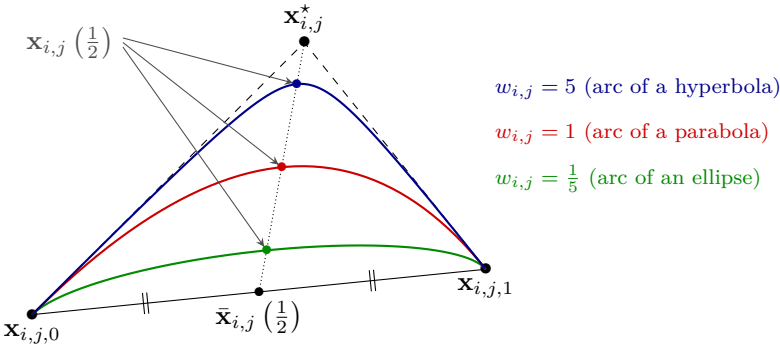


FIG. 4. Three rational Bézier arcs linking a start point $\mathbf{x}_{i,j,0}$ to an end point $\mathbf{x}_{i,j,1}$. Also shown are the control point $\mathbf{x}_{i,j}^*$ and weight $w_{i,j}$, along with the points $\bar{\mathbf{x}}_{i,j}(\frac{1}{2})$ and $\mathbf{x}_{i,j}(\frac{1}{2})$ that can be used for determining $w_{i,j}$.

311 Alternatively, the weight $w_{i,j}$ (when positive) relates to the absolute curvature κ of
 312 the conic section arc at its extremities $\mathbf{x}_{i,j,0}$ and $\mathbf{x}_{i,j,1}$ following [14]

$$313 \quad (3.43) \quad w_{i,j} = \sqrt{\frac{|\mathcal{A}(\mathbf{x}_{i,j,0}, \mathbf{x}_{i,j,1}, \mathbf{x}_{i,j}^*)|}{\kappa(\mathbf{x}_{i,j,0})\|\mathbf{x}_{i,j}^*\mathbf{x}_{i,j,0}\|^3}} = \sqrt{\frac{|\mathcal{A}(\mathbf{x}_{i,j,0}, \mathbf{x}_{i,j,1}, \mathbf{x}_{i,j}^*)|}{\kappa(\mathbf{x}_{i,j,1})\|\mathbf{x}_{i,j}^*\mathbf{x}_{i,j,1}\|^3}},$$

314 where κ at any point \mathbf{x} on the conic section is given by [17]

$$315 \quad (3.44) \quad \kappa(\mathbf{x}) = \frac{|(\mathbf{n}_i \times \nabla \phi(\mathbf{x})) \cdot (\mathbf{H}_\phi(\mathbf{n}_i \times \nabla \phi(\mathbf{x})))|}{\|\mathbf{n}_i \times \nabla \phi(\mathbf{x})\|},$$

316 with \mathbf{H}_ϕ the Hessian matrix

317 (3.45)
$$\mathbf{H}_\phi = 2 \begin{bmatrix} \alpha & 0 & 0 \\ 0 & \beta & 0 \\ 0 & 0 & 0 \end{bmatrix}.$$

318 Note that, in order to prevent round-off errors in the numerical calculation of $\mathcal{M}^{\tilde{\mathcal{P}}_3}$,
319 we limit our implementation to cases where $w_{i,j} \geq 0$. As a consequence, conic section
320 arcs that would result in negative rational Bézier weights are recursively split until
321 positive weights are found. With such a parametrization of the conic section arcs, it
322 can be shown that

323 (3.46)
$$\mathcal{M}_i^{\tilde{\mathcal{P}}_3} = \sum_{j=1}^{n_{\partial\tilde{\mathcal{F}}_i}} 1_{i,j}^{\partial\tilde{\mathcal{S}}} \mathcal{A}(\mathbf{x}_{i,j,0}, \mathbf{x}_{i,j,1}, \mathbf{x}_{i,j}^*) \mathcal{B}^{(3)}(w_{i,j}, \mathbf{x}_{i,j,0}, \mathbf{x}_{i,j,1}, \mathbf{x}_{i,j}^*) ,$$

324

325 where \mathcal{A} is the signed projected triangle area operator defined in Eq. (3.31) and the
326 operator $\mathcal{B}^{(3)} : \mathbb{R}^+ \times \mathbb{R}^3 \times \mathbb{R}^3 \times \mathbb{R}^3 \rightarrow \mathbb{R}^4$ is given in [Appendix A](#).

327 **3.4. A special elliptic case.** When $\alpha\beta > 0$ (i.e., \mathcal{S} is an elliptic paraboloid)
328 and the normal to \mathcal{F}_i is such that $\mathbf{n}_i \cdot \mathbf{e}_z \neq 0$, the intersection of the plane containing
329 the face \mathcal{F}_i with the surface \mathcal{S} is an ellipse. The intersection of \mathcal{F}_i with \mathcal{S} can then be:
330 empty, a collection of arcs of this ellipse, or the entire ellipse. In the latter case, the
331 sum of the contributions $\mathcal{M}_i^{\tilde{\mathcal{P}}_2}$ and $\mathcal{M}_i^{\tilde{\mathcal{P}}_3}$ can be directly calculated by integrating
332 $\Psi_{\mathcal{S}}$ and $\Psi_{\mathcal{F}_i}$ over the full ellipse, which yields the more concise expression

333 (3.47)
$$\mathcal{M}_i^{\tilde{\mathcal{P}}_2} + \mathcal{M}_i^{\tilde{\mathcal{P}}_3} = -\text{sign}(\mathbf{n}_i \cdot \mathbf{e}_z) \pi \frac{(\tau_i^2 \alpha + \lambda_i^2 \beta - 4\alpha\beta\delta_i)^2}{32(\alpha\beta)^{5/2}} \begin{bmatrix} 1 \\ \frac{\lambda_i}{2\alpha} \\ \frac{\tau_i}{2\beta} \\ \frac{5\tau_i^2}{12\beta} + \frac{5\lambda_i^2}{12\alpha} - \frac{2\delta_i}{3} \end{bmatrix} ,$$

334 where δ_i , λ_i , and τ_i have been defined in Eqs. (3.8)–(3.10). Note that this case only
335 occurs for $\mathbf{n}_i \cdot \mathbf{e}_z \neq 0$, hence these coefficients are here non-singular.

336 **4. Integrating on $\tilde{\mathcal{S}}$.** Although this manuscript is concerned with estimating
337 the first moments of $\tilde{\mathcal{P}}$, the integration domains and parametrizations introduced
338 in [Section 3](#) can also be used for integrating quantities associated with the clipped
339 surface $\tilde{\mathcal{S}}$, e.g., its moments. The area of $\tilde{\mathcal{S}}$, for instance, given as

340 (4.1)
$$M_0^{\tilde{\mathcal{S}}} = \int_{\tilde{\mathcal{S}}} 1 \, d\mathbf{x} ,$$

341

342 also reads after application of the divergence theorem as

343 (4.2)
$$M_0^{\tilde{\mathcal{S}}} = \sum_{i=1}^{n_{\mathcal{F}}} \sum_{j=1}^{n_{\partial\tilde{\mathcal{F}}_i}} -1_{i,j}^{\partial\tilde{\mathcal{S}}} \int_0^1 \gamma(x_{i,j}(t), y_{i,j}(t)) y'_{i,j}(t) \, dt ,$$

344

345 where

346 (4.3)
$$\gamma : \begin{cases} \mathbb{R}^2 & \rightarrow \mathbb{R} \\ (x, y) & \mapsto \int_0^x \sqrt{1 + 4\alpha^2 x^2 + 4\beta^2 y^2} \, dx \end{cases} .$$

347 The first moments of $\tilde{\mathcal{S}}$, as well as the average normal vector, average Gaussian
 348 curvature and average mean curvature of $\tilde{\mathcal{S}}$, for example, can be expressed similarly
 349 as sums of one-dimensional integrals over the parametric arcs of $\partial\tilde{\mathcal{S}}^\perp$. Contrary to the
 350 first moments of $\hat{\mathcal{P}}$, however, they need to be estimated using a numerical quadrature
 351 rule, as closed-form expressions cannot be derived.

352 **5. On floating-point arithmetics and robustness.** In the context of floating-
 353 point arithmetics, there exist cases for which the computed topology of the clipped
 354 faces $\hat{\mathcal{F}}_i$ may be ill-posed, preventing the accurate calculation of the moments of $\hat{\mathcal{P}}$.
 355 This occurs when, in the discrete sense:

- 356 1. The surface \mathcal{S} is tangent to one or more edges of the polyhedron \mathcal{P} ;
- 357 2. At least one corner or vertex of the polyhedron \mathcal{P} belongs to the surface \mathcal{S} .

358 For any given face of \mathcal{P} , the former case is numerically detected by computing the absolute
 359 value of the dot product between the normalized tangent to \mathcal{S} and the normalized
 360 edge from which the tangent originates, and checking whether it lies within $\epsilon_{\text{tangent}}$ of
 361 unity. The latter case is detected by checking whether the intersection of an edge with
 362 \mathcal{S} lies within ϵ_{corner} of a corner or vertex of the polyhedron \mathcal{P} . When any of these config-
 363urations is detected, the polyhedron \mathcal{P} is randomly translated and rotated about
 364 its centroid by a distance and an angle equal to ϵ_{nudge} , and the clipped face discrete
 365 topologies are re-computed. Moreover, we also switch to a higher-accuracy floating-
 366 point format, e.g., from a 64-bit to a 128-bit format. In the current work, where we
 367 aim to produce results in “double precision”, we find the values $\epsilon_{\text{nudge}} = 10^{10} \times \epsilon_{128}$,
 368 $\epsilon_{\text{corner}} = 10^2 \times \epsilon_{64}$, and $\epsilon_{\text{tangent}} = 10^6 \times \epsilon_{64}$, with $\epsilon_{64} = 2^{-52}$ and $\epsilon_{128} = 2^{-112}$ the upper
 369 bounds of the relative approximation error in 64-bit and 128-bit floating-point
 370 arithmetics, respectively, to prevent the computation of any ill-posed topologies in all
 371 tests presented in [Section 7](#) (for which more than 5×10^7 occurrences of the current
 372 “nudging” procedure are forced to occur). Choosing lower values for these tolerances
 373 may result in the generation of non-valid discrete topologies and/or erroneous
 374 moments. It should be noted that, for a polyhedron \mathcal{P} with volume $M_0^{\mathcal{P}} = \mathcal{O}(1)$, the rate
 375 of occurrence of the cases triggering this correction procedure is extremely small (that
 376 is, for non-engineered intersection configurations).

377 **6. Higher-order moments.** Second- and higher-order moments of the clipped
 378 polyhedron $\hat{\mathcal{P}}$ can be derived using the same procedure as presented in [Section 3](#) for
 379 the calculation of the zeroth and first moments. This merely entails appending higher-
 380 order monomials to the function vector Υ defined in Eq. [\(2.6\)](#). The arc parametriza-
 381 tions introduced in [Section 3](#) and used for calculating the three moment contributions
 382 $\mathcal{M}^{\hat{\mathcal{P}}_1}$, $\mathcal{M}^{\hat{\mathcal{P}}_2}$, and $\mathcal{M}^{\hat{\mathcal{P}}_3}$ would remain unchanged, while the operators $\mathcal{B}^{(1)}$, $\mathcal{B}^{(2)}$,
 383 and $\mathcal{B}^{(3)}$ would then contain additional components respectively corresponding to the
 384 monomials appended to Υ . We hypothesize that closed-form expressions similar to
 385 those given in [Section 3](#) can be derived for moments of $\hat{\mathcal{P}}$ of arbitrary order. However,
 386 these would involve an ever increasing amount of high-order monomials of α , β , and
 387 of the components of the vertices of $\hat{\mathcal{P}}$ and of the control points of the conic section
 388 arcs in $\partial\partial\hat{\mathcal{P}}$, rendering the computation of the moments more sensitive to round-off
 389 errors.

390 **7. Verification.** In this section, the closed-form expressions derived in [Section 3](#),
 391 the approach of [Section 4](#) for integrating on the clipped surface, and the corrective
 392 procedure of [Section 5](#) are tested on a wide variety of engineered and random inter-
 393 section configurations. When analytical expressions of the exact moments are not
 394 available, we recursively split the faces of the polyhedron \mathcal{P} so as to approximate

395 $\partial\mathcal{P} \cap \mathcal{Q}$ and $\partial\mathcal{P} \cap (\mathbb{R}^3 \setminus \mathcal{Q})$ by collections of oriented triangles. We refer to this procedure as the adaptive mesh refinement (AMR) of the faces of the polyhedron \mathcal{P} . We then exactly integrate Φ_S on the triangulated approximation of $\partial\mathcal{P} \cap (\mathbb{R}^3 \setminus \mathcal{Q})$ and $\Phi_{\mathcal{F}_i}$ on the triangulated approximation of each clipped face $\hat{\mathcal{F}}_i$, effectively approximating Eq. (3.11). For each case, we ensure that enough levels of recursive refinement are employed in order to reach machine-zero. Accumulated errors due to the summation of the contributions of all triangles are avoided by the use of compensated summation, also known as Kahan summation [20].

403 **7.1. Unit cube translating along e_z .** In a first test, we consider the elliptic
 404 paraboloid defined by Eq. (2.2) with $\alpha = \beta = 1$, intersecting with the unit cube
 405 centered at $\mathbf{x}_c = [1/2 \ 1/2 \ 1/2 - k]^\top$ (as illustrated in Figure 5). For this case, the
 406 zeroth and first moments of $\hat{\mathcal{P}}$, as well as the zeroth moment of $\tilde{\mathcal{S}}$, can be derived as
 407 analytical functions of k^\dagger . We compare these exact moments against those computed
 408 using the closed-form expressions derived in Section 3 for estimating the moments
 409 of $\hat{\mathcal{P}}$, and by integrating Eq. (4.2) numerically with an adaptive Gauss-Legendre
 410 quadrature rule for estimating the zeroth moment of $\tilde{\mathcal{S}}$. The parameter k is regularly
 411 sampled on $[0, 3]$ with a uniform spacing $\Delta k = 10^{-3}$.

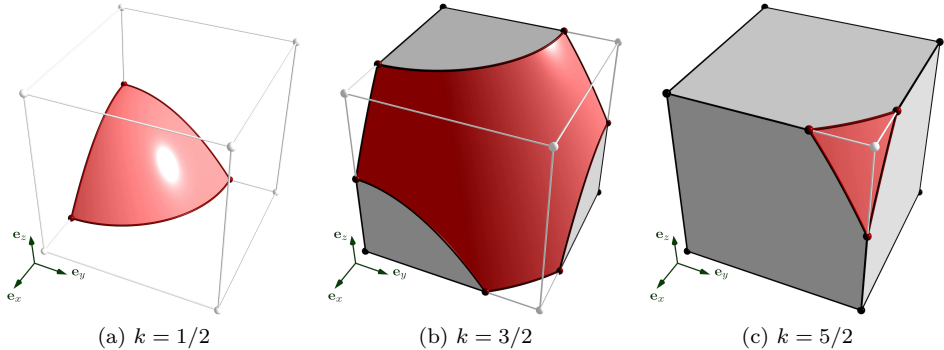


FIG. 5. Unit cube centred at $[1/2 \ 1/2 \ 1/2 - k]^\top$ clipped by the elliptic paraboloid parametrically defined as $z = -x^2 - y^2$.

412 The left-hand graph of Figure 6 shows the exact moments of $\hat{\mathcal{P}}$, scaled by their maxi-
 413 mum values, as well as the exact zeroth moment of $\tilde{\mathcal{S}}$, scaled by its value at $k = 1$. The
 414 right-hand side of Figure 6 shows the errors associated with their estimation, scaled
 415 similarly. These errors are all contained within an order of magnitude of $\epsilon_{64} = 2^{-52}$,
 416 the upper bound of the relative approximation error in 64-bit floating-point arith-
 417 metics.

418 **7.2. Parameter sweep for several geometries.** In a second test, we consider
 419 a selection of convex polyhedra (a regular tetrahedron, a cube, and a regular do-
 420 decahedron) and non-convex polyhedra (a hollow cube and the triangulated Stanford
 421 bunny [29]). These polyhedra, whose properties are summarized in Table 1, are scaled
 422 so as to have a unit volume (i.e., $M_0^{\mathcal{P}} = 1$), and a centroid initially located at the ori-
 423 gin (i.e., $M_1^{\mathcal{P}} = \mathbf{0}$). They are then translated along $\mathbf{t} = [t_x \ t_y \ t_z]^\top$, and rotated

[†]A C++ implementation of these functions can be found at the beginning of `/tests/src/paraboloid_intersection_test.cpp` in the open-source Interface Reconstruction Library.

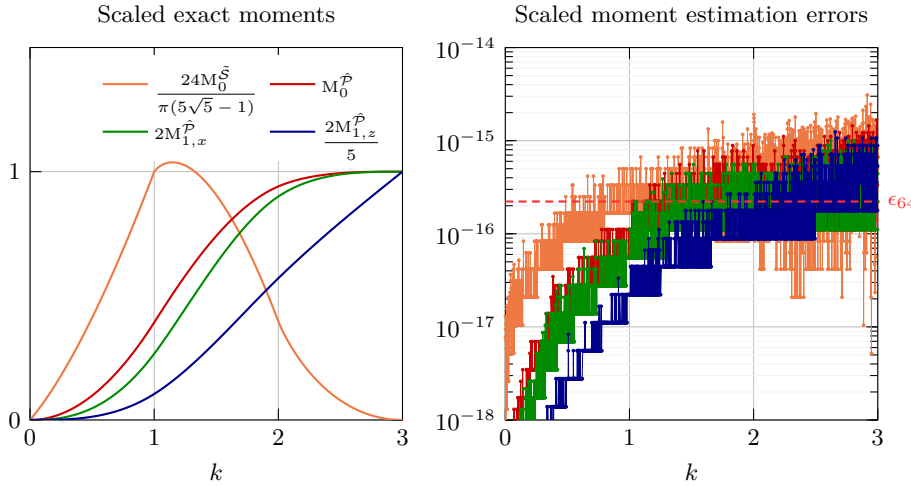


FIG. 6. Moments of the unit cube centred at $[1/2 \ 1/2 \ 1/2 - k]^\top$ clipped by the elliptic paraboloid parametrically defined as $z = -x^2 - y^2$, and the error in their estimation with 64-bit floating point arithmetics. The volume moments and their estimation errors are scaled with respect to the moments at $k = 3$. The surface area and its estimation error is scaled with respect to the surface area at $k = 1$. The volume moments are computed from the analytical expressions derived in Section 3, whereas the surface area is computed from Eq. (4.2) using an adaptive Gauss-Legendre quadrature rule. The 64-bit machine-epsilon $\epsilon_{64} = 2^{-52}$ is shown as the dashed red line.

TABLE 1

Five polyhedra are considered: a regular tetrahedron, a cube, a regular dodecahedron, a hollow cube, and the triangulated Stanford bunny [29]. The first three polyhedra are convex, whereas the last two are not. The hollow cube contains non-convex faces.

Geometry	Tetrahedron	Cube	Dodecahedron	Hollow cube	Stanford bunny
Number of vertices	4	8	20	16	167,891
Number of faces	4	6	12	12	335,778
Are all faces convex?	Yes	Yes	Yes	No	Yes
Is polyhedron convex?	Yes	Yes	Yes	No	No
Snapshot					

424 about the three basis vectors $(\mathbf{e}_x, \mathbf{e}_y, \mathbf{e}_z)$ with the angles θ_x , θ_y , and θ_z , respectively.
425 Throughout this section, (t_x, t_y, t_z) are varied in $[-\frac{1}{2}, \frac{1}{2}]^3$, $(\theta_x, \theta_y, \theta_z)$ are varied in
426 $[-\pi, \pi]^3$, and the paraboloid coefficients (α, β) are varied in $[-5, 5]^2$.

427 A random parameter sweep is first conducted by uniform random sampling of the
428 eight parameters $(t_x, t_y, t_z, \theta_x, \theta_y, \theta_z, \alpha, \beta)$ in the parameter space $[-\frac{1}{2}, \frac{1}{2}]^3 \times [-\pi, \pi]^3 \times$
429 $[-\frac{1}{2}, \frac{1}{2}]^2$, totalling more than 2×10^8 realizations. A graded parameter sweep is then
430 conducted, in which the eight parameters are chosen in the discrete parameter space
431 $\{-\frac{1}{2}, -\frac{1}{4}, 0, \frac{1}{4}, \frac{1}{2}\}^3 \times \{-\pi, -\frac{\pi}{2}, 0, \frac{\pi}{2}, \pi\}^3 \times \{-5, -4, \dots, 4, 5\}^2$, resulting in $5^3 \times 5^3 \times 11^2 =$

432 1,890,625 distinct realizations for each geometry[‡]. The graded parameter sweep
 433 differs from the random one in that it raises many singular intersection configurations
 434 (e.g., degenerate conic sections that consist of parallel or intersecting line segments,
 435 or conic sections that are parabolas) and/or ambiguous discrete topologies that arise
 436 from polyhedron vertices lying on the paraboloid or edges of the polyhedron being
 437 tangent to the paraboloid, therefore testing the robustness of our implementation as
 438 well as of the procedure described in [Section 5](#). For each case of the random and graded
 439 parameter sweeps, the reference value of $\mathcal{M}^{\hat{\mathcal{P}}}$ for calculating the moment errors is
 440 obtained by adaptive mesh refinement (AMR) of the faces of \mathcal{P} into triangles, followed
 441 by the (exact) integration of Φ_S and $\Phi_{\mathcal{F}_i}$, given in Eq. [\(3.12\)](#), over the triangles above
 442 and below the paraboloid, respectively. Examples of random intersection cases and
 443 their associated AMR are shown in [Figure 7](#), whereas examples of singular cases raised
 444 during the graded parameter sweep are shown in [Figure 8](#).

445 The maximum and average moment errors obtained during the random parameter
 446 sweep are given in [Table 2](#). For the tetrahedron, cube, dodecahedron, and hollow
 447 cube, the average moment error is of the order $\epsilon_{64} = 2^{-52} \sim \mathcal{O}(10^{-16})$, whereas the
 448 maximum error is about one to two orders of magnitude larger. The average and
 449 maximum moment errors for the Stanford bunny, which contains $\mathcal{O}(10^5)$ faces, are
 450 each about one order of magnitude larger than for the other polyhedra but still close
 451 to machine-zero. The graded parameter sweep, whose results are given in [Table 3](#),
 452 exhibits similar moment errors as for the random parameter sweep, even though,
 453 by design, it raises many more singular intersection configurations and ambiguous
 454 discrete topologies than the random parameter sweep, therefore requiring a more
 455 frequent use of the nudging procedure described in [Section 5](#).

TABLE 2

Random parameter sweep results. For each geometry, we provide: the number of tests conducted, the number of recursive levels used for the AMR reference moment calculation, as well as the average and maximum errors in the estimation of the zeroth and first moments.

Geometry	Number of tests	AMR levels	Zeroth moment error		First moments error	
			Average	Maximum	Average	Maximum
Tetrahedron	5×10^7	17	2.3×10^{-16}	3.8×10^{-15}	1.6×10^{-16}	6.9×10^{-14}
Cube	5×10^7	17	2.4×10^{-16}	2.5×10^{-15}	8.7×10^{-17}	2.1×10^{-14}
Dodecahedron	5×10^7	17	3.5×10^{-16}	1.9×10^{-15}	6.8×10^{-17}	6.2×10^{-15}
Hollow cube	5×10^7	17	2.0×10^{-16}	3.2×10^{-15}	1.3×10^{-16}	3.4×10^{-14}
Stanford bunny	1×10^3	13	5.8×10^{-15}	4.8×10^{-14}	2.7×10^{-15}	3.1×10^{-14}

TABLE 3

Graded parameter sweep results. For each geometry, we provide: the number of tests conducted, the number of recursive levels used for the AMR reference moment calculation, as well as the average and maximum errors in the estimation of the zeroth and first moments.

Geometry	Number of tests	AMR levels	Zeroth moment error		First moments error	
			Average	Maximum	Average	Maximum
Tetrahedron	$5^6 \times 11^2$	22	2.7×10^{-16}	4.9×10^{-15}	2.1×10^{-16}	3.9×10^{-14}
Cube	$5^6 \times 11^2$	22	2.6×10^{-16}	4.7×10^{-15}	1.0×10^{-16}	2.1×10^{-14}
Dodecahedron	$5^6 \times 11^2$	22	3.7×10^{-16}	1.7×10^{-15}	8.3×10^{-17}	5.4×10^{-15}
Hollow cube	$5^6 \times 11^2$	22	2.0×10^{-16}	4.2×10^{-15}	1.6×10^{-16}	4.8×10^{-14}

[‡]We do not present the results of a graded parameter sweep on the Stanford bunny, since the “organic” nature of this polyhedron renders a graded parameter sweep equivalent to a random one.

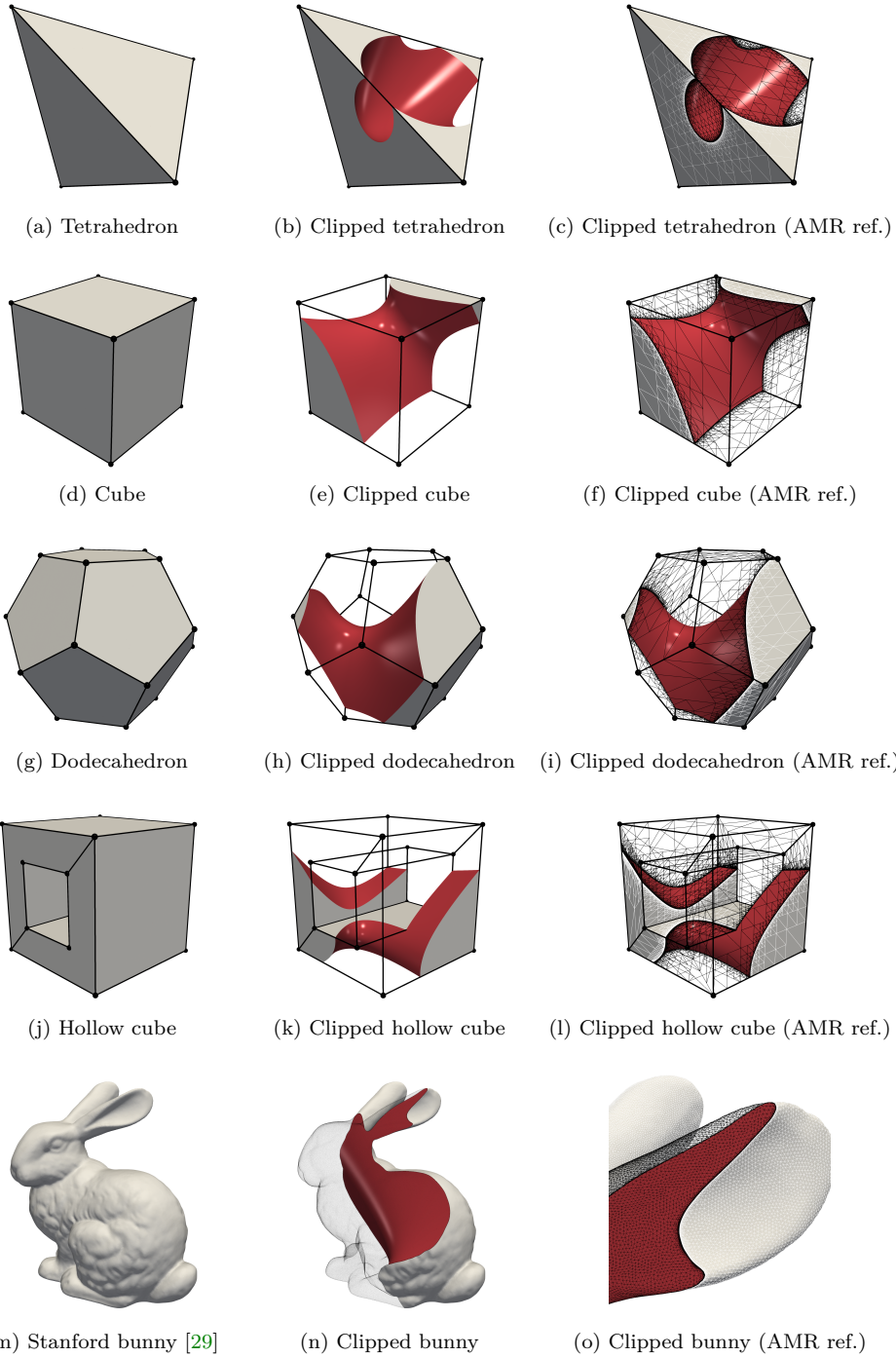


FIG. 7. Examples of random intersection cases between the five considered polyhedra and a paraboloid. The left column shows the full polyhedra; the central column shows the polyhedra clipped by a paraboloid; the right column shows the edges of the AMR of the polyhedra used for calculating the reference moments.

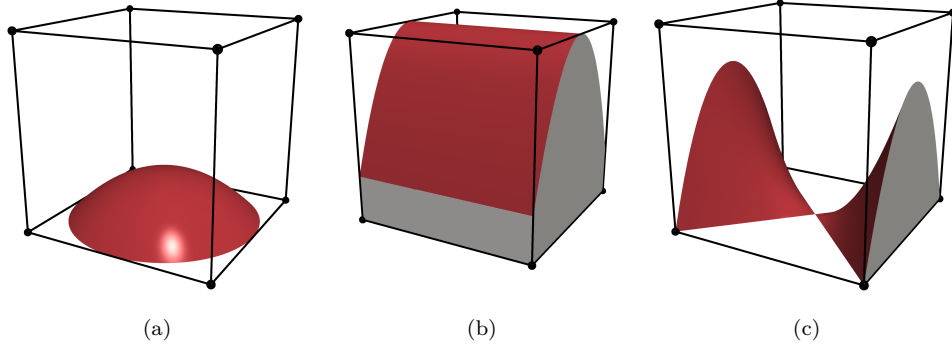


FIG. 8. Examples of cases with singular intersection configurations and/or ambiguous topologies covered by the graded parameter sweep: (a) the elliptic paraboloid is tangent to four edges of the polyhedron; (b) the parabolic cylinder is tangent to one face of the polyhedron, resulting in a degenerate conic section intersection that is made of two overlapping parallel lines; (c) the intersection of the hyperbolic paraboloid with one face of the polyhedron results in a degenerate hyperbola that is the intersection of two straight lines.

7.3. Parameter sweep with nudge. In order to further test the robustness of our implementation and of the nudging procedure described in Section 5, we consider the same random parameter sweep for the cube geometry as described in Subsection 7.2, but with the addition of a post-sample translation of the polyhedron along \mathbf{e}_z so as for one of its vertices to lie exactly on the paraboloid. At least one iteration of the nudging procedure of Section 5 is therefore required for each random sample. The results of this random parameter sweep are given in Table 4, displaying numbers of a similar order of magnitude as for the random parameter sweep presented in Subsection 7.2.

TABLE 4

Random parameter sweep with one vertex of the polyhedron lying exactly on the paraboloid. We provide: the number of tests conducted, the number of recursive levels used for the AMR reference moment calculation, as well as the average and maximum errors in the estimation of the zeroth and first moments.

Geometry	Number of tests	AMR levels	Zeroth moment error		First moments error	
			Average	Maximum	Average	Maximum
Cube (vertex on \mathcal{S})	5×10^7	17	2.4×10^{-16}	7.8×10^{-15}	1.8×10^{-16}	4.5×10^{-14}

7.4. Timings. In order to assess the performances of our implementation, the time required for each moment estimation of the random parameter sweeps presented in Subsections 7.2 and 7.3 has been measured using OpenMP’s `omp_get_wtime()` function [9], which has a precision of 1 nanosecond on the workstation that we used. The characteristics of this workstation are summarized in Table 5. The C++ code implementing the closed-form expressions presented in Section 3 has been compiled with the GNU 10.3.0 suite of compilers [1], using the flags given in Table 5. The timings are summarized in Table 6, which shows the average moment calculation time for the zeroth moment only, and for both the zeroth and first moments. Overall, the average time for calculating the first moments of a polyhedron clipped by a paraboloid is less than 1 μ s per face of the original polyhedron. A direct comparison

TABLE 5

Characteristics of the workstation used for the timing results presented in Subsection 7.4 (this is the same workstation as used in [8]).

CPU	vendor_id	GenuineIntel
	CPU family	6
	Model	158
	Model name	Intel(R) Core(TM) i7-8700K CPU 3.70 GHz
	Stepping	10
	Microcode	0xca
	Min/max clock CPU frequency	800 MHz – 4.70 GHz
	CPU asserted frequency	4.0 GHz
	Cache size	12288 KB
Compiler	Suite	GNU
	Version	10.3.0
	Flags	-O3 -march=native -DNDEBUG -DNDEBUG_PERF*

* -DNDEBUG_PERF is an IRL-specific compiler flag that disables additional debugging assertions [8].

476 can be made with the half-space clipping of [8], which used the same workstation
 477 as the current work. It transpires that the clipping of a cube by a paraboloid is on
 478 average less than 6 times more expensive than its clipping by a plane. When the
 479 nudging procedure of Section 5 is required, as is the case for each realization of the
 480 modified random parameter sweep presented in Subsection 7.3, the timings of which
 481 are shown in the last row of Table 6, an increase in cost by a factor of about 200 is
 482 observed. This is mostly due to the switch to quadruple precision that is operated
 483 in conjunction with the random translation and rotation of the polyhedron by a value
 484 of ϵ_{nudge} . It should be noted that such cases occur extremely rarely, unless they are
 485 manually engineered as in Subsection 7.3.

TABLE 6

Timings for the random parameter sweeps presented in Subsections 7.2 and 7.3. The timings measured in [8] for the clipping of a cube by a plane are provided for reference (they were measured on the same workstation as used for the current work).

Geometry	Number of tests	Average moment calculation time			
		Zeroth moment only		Zeroth and first moments	
		$\mu\text{s/test}$	$\mu\text{s/test/face}$	$\mu\text{s/test}$	$\mu\text{s/test/face}$
Tetrahedron	5×10^7	1.07	0.27	1.89	0.47
Cube	5×10^7	1.57	0.26	2.53	0.42
Cube (half-space clipping) [8]	15×10^6	0.27	0.05	--	--
Dodecahedron	5×10^7	2.66	0.22	3.96	0.33
Hollow cube	5×10^7	3.27	0.27	5.12	0.43
Stanford bunny	1×10^3	6.22×10^4	0.19	6.41×10^4	0.19
Cube (vertex on \mathcal{S})	5×10^7	236	39.3	541	90.2

486 **8. Conclusions.** We have derived closed-form expressions for the first moments
 487 of a polyhedron clipped by a paraboloid, enabling their robust machine-accurate esti-
 488 mation at a computational cost that is considerably lower than with any other avail-
 489 able approach. These expressions have been obtained by consecutive applications
 490 of the divergence theorem, transforming the three-dimensional integrals that are the
 491 zeroth and first moments of the clipped polyhedron into a sum of one-dimensional

integrals. This requires parametrizing the conic section arcs resulting from the intersection of the paraboloid with the polyhedron's faces, which we have chosen to express as rational quadratic Bézier curves. The moments of the clipped polyhedron can, as a result, be expressed as the sum of three main contributions that are function of the polyhedron vertices and of the coefficients of the paraboloid. These expressions do not differ based on the type of paraboloid that is considered (elliptic, hyperbolic, or parabolic). Making use of this parametrization, we also show how to express integrals over the curved faces of the clipped polyhedron as the sums of one-dimensional integrals. When ambiguous discrete intersection topologies are detected, e.g., when the paraboloid is tangent to an edge of the polyhedron or intersects the polyhedron at the location of one of its vertices, a nudging procedure is triggered so as to guarantee robust moment estimations. A series of millions of intersection configurations that are randomly chosen, as well as manually engineered so as to raise singular intersection configurations and/or ambiguous discrete topologies, have been tested. These showcase an average moment estimation error that is of the order of the machine-zero, and a maximum error that is about one order of magnitude larger. The timing of these moment estimations shows that the clipping of a polyhedron by a paraboloid, with our approach, is on average about 6 times more expensive than its clipping by a plane.

Reproducibility. The code used to produce the results presented in this manuscript is openly available as part of the [Interface Reconstruction Library \(IRL\)](#). A [step-by-step guide](#) for reproducing the figures and tables of this manuscript using IRL can be found in the library's documentation. The commit hash corresponding to the version of the code used in this manuscript is [8e77b35](#).

Acknowledgments. This project has received funding from the European Union's Horizon 2020 research and innovation programme under the Marie Skłodowska-Curie grant agreement No 101026017 . Robert Chiodi was sponsored by the Office of Naval Research (ONR) as part of the Multidisciplinary University Research Initiatives (MURI) Program, under grant number N00014-16-1-2617. The views and conclusions contained herein are those of the authors only and should not be interpreted as representing those of ONR, the U.S. Navy or the U.S. Government.

Appendix A. Third contribution to the moments. The third contribution to the moments of face \mathcal{F}_i , $\mathcal{M}_i^{\hat{\mathcal{P}}_3}$, is obtained by calculating the integral on the right-hand side of Eq. (3.26) using the definitions in Eqs. (3.12), (3.14), and (3.15), as well as the facts that $\forall j \in \{1, \dots, n_{\partial\hat{\mathcal{F}}_i}\}$,

$$527 \quad (A.1) \quad z_{i,j} = \delta_i - \lambda_i x_{i,j} - \tau_i y_{i,j},$$

$$528 \quad (A.2) \quad 1_{i,j}^{\partial\hat{\mathcal{S}}} \neq 0 \Leftrightarrow \begin{cases} z_{i,j,0} = -\alpha x_{i,j,0}^2 - \beta y_{i,j,0}^2 \\ z_{i,j,1} = -\alpha x_{i,j,1}^2 - \beta y_{i,j,1}^2 \end{cases},$$

530 and that the control point $\mathbf{x}_{i,j}^*$ belongs to the plane containing the face \mathcal{F}_i hence

$$531 \quad (A.3) \quad z_{i,j}^* = \delta_i - \lambda_i x_{i,j}^* - \tau_i y_{i,j}^*.$$

533 After substitution of these expressions in Eq. (3.26) and some simplification, $\mathcal{M}_i^{\hat{\mathcal{P}}_3}$
534 can be shown to read as in Eq. (3.46), with

$$535 \quad (A.4) \quad \mathcal{B}^{(3)}(w, \mathbf{x}_a, \mathbf{x}_b, \mathbf{x}_c) = \text{diag}(\mathcal{E}(w)) (\mathcal{C}(\mathbf{x}_a, \mathbf{x}_b, \mathbf{x}_c) \mathcal{K}\mathcal{D}(w)),$$

536 where: \mathcal{C} is a 4×12 matrix whose non-zero coefficients contributing to $\mathbf{M}_0^{\hat{P}}$ are given
 537 as

$$538 \quad (A.5) \quad \mathcal{C}_{1,1} = \alpha(x_a^2 + 2x_ax_b + x_b^2) + \beta(y_a^2 + 2y_ay_b + y_b^2) - 2z_a - 2z_b,$$

$$539 \quad (A.6) \quad \begin{aligned} \mathcal{C}_{1,2} &= \alpha(x_a^2 + 2x_ax_b + x_b^2 + 4x_ax_c + 4x_bx_c + 4x_c^2) \\ &\quad + \beta(y_a^2 + 2y_ay_b + y_b^2 + 4y_ay_c + 4y_by_c + 4y_c^2) \\ &\quad - 4z_a - 4z_b - 8z_c, \end{aligned}$$

$$542 \quad (A.7) \quad \mathcal{C}_{1,3} = \alpha x_c^2 + \beta y_c^2 - z_c,$$

544 whose non-zero coefficients contributing to $\mathbf{e}_x \cdot \mathbf{M}_1^{\hat{P}}$ are given as

$$\begin{aligned} 545 \quad (A.8) \quad \mathcal{C}_{2,4} &= \beta(-12x_ay_ay_b + 12x_ay_b^2 + 12x_by_a^2 - 12x_by_ay_b) \\ &\quad - 6x_az_a + 6x_ay_b + 6x_bz_a - 6x_bz_b, \\ 547 \quad (A.9) \quad \mathcal{C}_{2,5} &= \alpha(-12x_ax_c^2 + 60x_ax_cx_b - 12x_c^2x_b) \\ &\quad + \beta(28x_ay_ay_c - 8x_ay_ay_b - 4x_ay_c^2 + 20x_ay_cy_b + 8x_ay_b^2 \\ &\quad - 28x_cy_a^2 - 8x_cy_ay_c + 20x_cy_ay_b - 8x_cy_cy_b - 28x_cy_b^2 \\ &\quad + 8x_by_a^2 + 20x_by_ay_c - 8x_by_ay_b - 4x_by_c^2 + 28x_by_cy_b) \\ &\quad + 10x_az_a + 20x_ay_b + 14x_ay_c - 22x_cz_a - 8x_cz_c \\ &\quad - 22x_cz_b + 14x_bz_a + 20x_bz_c + 10x_bz_b, \\ 553 \quad (A.10) \quad \mathcal{C}_{2,6} &= \alpha(-36x_ax_c^2 + 12x_ax_cx_b + 12x_c^3 - 36x_c^2x_b) \\ &\quad + \beta(-12x_ay_c^2 + 4x_ay_cy_b - 24x_cy_ay_c + 4x_cy_a \\ &\quad y_b + 12x_cy_c^2 - 24x_cy_cy_b + 4x_by_ay_c - 12x_by_c^2) \\ &\quad - 10x_az_c + 2x_ay_b + 10x_cz_a - 12x_cz_c - 10x_cz_b \\ &\quad + 2x_bz_a - 10x_bz_c, \\ 558 \quad (A.11) \quad \mathcal{C}_{2,7} &= 2\alpha x_c^3 + 2\beta x_cy_c^2 + 2x_cz_c, \end{aligned}$$

560 whose non-zero coefficients contributing to $\mathbf{e}_y \cdot \mathbf{M}_1^{\hat{P}}$ are given as

$$561 \quad (A.12) \quad \begin{aligned} \mathcal{C}_{3,4} &= \alpha(12x_a^2y_b - 12x_ax_by_a - 12x_ax_by_b + 12x_b^2y_a) \\ &\quad - 6y_az_a + 6y_ay_b + 6y_bz_a - 6y_bz_b \end{aligned}$$

$$\begin{aligned} 563 \quad (A.13) \quad \mathcal{C}_{3,5} &= \alpha(-28x_a^2y_c + 8x_a^2y_b + 28x_ax_cy_a - 8x_ax_cy_c + 20x_ax_cy_b \\ &\quad - 8x_ax_by_a + 20x_ax_by_c - 8x_ax_by_b - 4x_c^2y_a - 4x_c^2y_b \\ &\quad + 20x_cx_by_a - 8x_cx_by_c + 28x_cx_by_b + 8x_b^2y_a - 28x_b^2y_c) \\ &\quad + \beta(-12y_ay_c^2 + 60y_ay_cy_b - 12y_c^2y_b) \\ &\quad + 10y_az_a + 20y_ay_b + 14y_ay_c - 22y_cz_a - 8y_cz_c \\ &\quad - 22y_cz_b + 14y_bz_a + 20y_bz_c + 10y_bz_b, \end{aligned}$$

$$\begin{aligned} 569 \quad (A.14) \quad \mathcal{C}_{3,6} &= \alpha(-24x_ax_cy_c + 4x_ax_cy_b + 4x_ax_by_c - 12x_c^2y_a \\ &\quad + 12x_c^2y_c - 12x_c^2y_b + 4x_cx_by_a - 24x_cx_by_c) \\ &\quad + \beta(-36y_ay_c^2 + 12y_ay_cy_b + 12y_c^3 - 36y_c^2y_b) \\ &\quad - 10y_az_c + 2y_ay_b + 10y_cz_a - 12y_cz_c - 10y_cz_b \\ &\quad + 2y_bz_a - 10y_bz_c, \end{aligned}$$

574 (A.15) $\mathcal{C}_{3,7} = 2\alpha x_c^2 y_c + 2\beta y_c^3 + 2y_c z_c ,$

576 and whose non-zero coefficients contributing to $\mathbf{e}_z \cdot \mathbf{M}_1^P$ are given as

577 (A.16) $\mathcal{C}_{4,8} = +\alpha\beta (-42y_a^2 x_a^2 - 10y_b^2 x_a^2 - 28y_a y_b x_a^2 - 28x_b y_a^2 x_a$
 578 $- 28x_b y_b^2 x_a - 40x_b y_a y_b x_a - 10x_b^2 y_a^2 - 42x_b^2 y_b^2 - 28x_b^2 y_a y_b)$
 579 $+ \alpha^2 (-21x_a^4 - 28x_b x_a^3 - 30x_b^2 x_a^2 - 28x_b^3 x_a - 21x_b^4)$
 580 $+ \beta^2 (-21y_a^4 - 28y_b y_a^3 - 30y_b^2 y_a^2 - 28y_b^3 y_a - 21y_b^4)$
 581 $40z_a^2 + 40z_b^2 + 48z_a z_b ,$

582 (A.17) $\mathcal{C}_{4,9} = \alpha\beta (-7y_c^2 x_a^2 - 10y_b^2 x_a^2 + 63y_a y_c x_a^2 - 21y_a y_b x_a^2 + 35y_c y_b x_a^2$
 583 $+ 63x_c y_a^2 x_a - 21x_b y_a^2 x_a - 10x_b y_c^2 x_a + 35x_c y_b^2 x_a$
 584 $- 21x_b y_b^2 x_a - 28x_c y_a y_c x_a + 70x_b y_a y_c x_a + 70x_c y_a y_b x_a$
 585 $- 40x_b y_a y_b x_a - 20x_c y_c y_b x_a + 70x_b y_c y_b x_a - 7x_c^2 y_a^2$
 586 $- 10x_b^2 y_a^2 + 35x_c x_b y_a^2 - 7x_b^2 y_c^2 - 7x_c^2 y_b^2 + 63x_c x_b y_b^2$
 587 $+ 35x_b^2 y_a y_c - 20x_c x_b y_a y_c - 10x_c^2 y_a y_b - 21x_b^2 y_a y_b$
 588 $+ 70x_c x_b y_a y_b + 63x_b^2 y_c y_b - 28x_c x_b y_c y_b)$

589 $+ \alpha^2 (63x_c x_a^3 - 21x_b x_a^3 - 21x_c^2 x_a^2 - 30x_b^2 x_a^2 + 105x_c x_b x_a^2$
 590 $- 21x_b^3 x_a + 105x_c x_b^2 x_a - 30x_c^2 x_b x_a + 63x_c x_b^3 - 21x_c^2 x_b^2)$
 591 $+ \beta^2 (63y_c y_a^3 - 21y_b y_a^3 - 21y_c^2 y_a^2 - 30y_b^2 y_a^2 + 105y_c y_b y_a^2$
 592 $- 21y_b^3 y_a + 105y_c y_b^2 y_a - 30y_c^2 y_b y_a + 63y_c y_b^3 - 21y_c^2 y_b^2)$
 593 $- 30z_a^2 + 12z_c^2 - 30z_b^2 - 60z_a z_c - 24z_a z_b - 60z_c z_b ,$

594 (A.18) $\mathcal{C}_{4,10} = \alpha\beta (-56y_c^2 x_a^2 - 2y_b^2 x_a^2 + 28y_c y_b x_a^2 + 84x_c y_c^2 x_a$
 595 $- 92x_b y_c^2 x_a + 28x_c y_b^2 x_a - 224x_c y_a y_c x_a + 56x_b y_a y_c x_a$
 596 $+ 56x_c y_a y_b x_a - 8x_b y_a y_b x_a - 184x_c y_c y_b x_a$
 597 $+ 56x_b y_c y_b x_a - 56x_c^2 y_a^2 - 2x_b^2 y_a^2 + 28x_c x_b y_a^2$
 598 $- 12x_c^2 y_c^2 - 56x_b^2 y_c^2 + 84x_c x_b y_c^2 - 56x_c^2 y_b^2$
 599 $+ 84x_c^2 y_a y_c + 28x_b^2 y_a y_c - 184x_c x_b y_a y_c$
 600 $- 92x_c^2 y_a y_b + 56x_c x_b y_a y_b + 84x_c^2 y_c y_b - 224x_c x_b y_c y_b)$
 601 $+ \alpha^2 (-6x_c^4 + 84x_a x_c^3 + 84x_b x_c^3 - 168x_a^2 x_c^2 - 168x_b^2 x_c^2$
 602 $- 276x_a x_b x_c^2 + 84x_a x_b^2 x_c + 84x_a^2 x_b x_c - 6x_a^2 x_b^2)$
 603 $+ \beta^2 (-6y_c^4 + 84y_a y_c^3 + 84y_b y_c^3 - 168y_a^2 y_c^2 - 168y_b^2 y_c^2$
 604 $- 276y_a y_b y_c^2 + 84y_a y_b^2 y_c + 84y_a^2 y_b y_c - 6y_a^2 y_b^2)$
 605 $+ 15z_a^2 + 24z_c^2 + 15z_b^2 + 120z_a z_c - 6z_a z_b + 120z_c z_b ,$

606 (A.19) $\mathcal{C}_{4,11} = \alpha\beta (-12y_c^2 x_c^2 + 14y_a y_c x_c^2 - 2y_a y_b x_c^2$
 607 $+ 14y_c y_b x_c^2 + 14x_a y_c^2 x_c + 14x_b y_c^2 x_c$
 608 $- 4x_b y_a y_c x_c - 4x_a y_c y_b x_c - 2x_a x_b y_c^2)$
 609 $+ \alpha^2 (-6x_c^4 + 14x_a x_c^3 + 14x_b x_c^3 - 6x_a x_b x_c^2)$
 610 $+ \beta^2 (-6y_c^4 + 14y_a y_c^3 + 14y_b y_c^3 - 6y_a y_b y_c^2)$
 611 $- 7z_c^2 - 5z_a z_c + z_a z_b - 5z_c z_b ,$

613 (A.20) $\mathcal{C}_{4,12} = -2\alpha\beta y_c^2 x_c^2 - \alpha^2 x_c^4 - \beta^2 y_c^4 + z_c^2 ;$

614 \mathcal{K} is the 12×10 matrix given as

615 (A.21) $\mathcal{K} = \begin{bmatrix} -\frac{3}{8} & \frac{31}{48} & -\frac{7}{8} & -\frac{1}{16} & 0 & \frac{1}{24} & 0 & 0 & 0 & 0 \\ 0 & -\frac{1}{6} & \frac{5}{8} & -\frac{3}{16} & 0 & \frac{1}{24} & 0 & 0 & 0 & 0 \\ 0 & \frac{2}{3} & -3 & \frac{11}{6} & -2 & 0 & 0 & 0 & 0 & 0 \\ -\frac{1}{32} & \frac{93}{2240} & 0 & -\frac{163}{3360} & 0 & \frac{5}{168} & 0 & -\frac{1}{140} & 0 & 0 \\ 0 & \frac{1}{70} & -\frac{1}{16} & \frac{29}{1120} & 0 & -\frac{19}{1680} & 0 & \frac{1}{420} & 0 & 0 \\ 0 & -\frac{1}{210} & 0 & \frac{1}{21} & -\frac{1}{8} & \frac{13}{560} & 0 & -\frac{1}{280} & 0 & 0 \\ 0 & \frac{1}{35} & 0 & -\frac{16}{105} & 0 & \frac{56}{105} & -1 & \frac{1}{14} & 0 & 0 \\ -\frac{1}{128} & \frac{193}{16128} & 0 & -\frac{149}{8064} & 0 & \frac{19}{1120} & 0 & \frac{41}{5040} & 0 & \frac{1}{630} \\ 0 & \frac{4}{945} & -\frac{1}{48} & \frac{65}{6048} & 0 & -\frac{1}{144} & 0 & \frac{11}{3780} & 0 & -\frac{1}{1890} \\ 0 & -\frac{1}{1890} & 0 & \frac{13}{1890} & -\frac{1}{48} & \frac{11}{2016} & 0 & -\frac{5}{3024} & 0 & \frac{1}{3780} \\ 0 & \frac{1}{315} & 0 & -\frac{1}{45} & 0 & \frac{4}{35} & -\frac{1}{4} & \frac{17}{504} & 0 & -\frac{1}{252} \\ 0 & -\frac{1}{63} & 0 & \frac{29}{315} & 0 & -\frac{26}{105} & 0 & \frac{194}{315} & -1 & \frac{1}{18} \end{bmatrix} ;$

616 \mathcal{D} is the vector given as

617 (A.22) $\mathcal{D}(w) = \begin{bmatrix} 0 & w^2 & 0 & w^4 & 0 & w^6 & 0 & w^8 & 0 & w^{10} \end{bmatrix}^\top$
 618 $+ \Theta(w) \begin{bmatrix} w & 0 & w^3 & 0 & w^5 & 0 & w^7 & 0 & w^9 & 0 \end{bmatrix}^\top ;$
 619

620 and \mathcal{E} is the vector given as

621 (A.23) $\mathcal{E}(w) = \begin{bmatrix} \Lambda(w)^3 & \Lambda(w)^4 & \Lambda(w)^4 & \Lambda(w)^5 \end{bmatrix}^\top ,$

622 with

623 (A.24) $\Theta(w) = \begin{cases} \arctan\left(\frac{1-w}{\sqrt{1-w^2}}\right) \frac{1}{\sqrt{1-w^2}} & 0 < w < 1 \\ \operatorname{arctanh}\left(\frac{w-1}{\sqrt{w^2-1}}\right) \frac{1}{\sqrt{w^2-1}} & 1 \leq w \end{cases} ,$

624 (A.25) $\Lambda(w) = \frac{1}{(w-1)(w+1)} .$
 625

626 It should be noted that the naive implementation of these expressions may lead to
 627 significant round-off errors when w is in the vicinity of 1. To avoid such problems,
 628 we resort to the Taylor series expansion of $\mathcal{B}^{(3)}$ around $w = 1$ for its numerical
 629 estimation. Using 64-bit floating-point arithmetics, we have found that the Taylor
 630 series expansion of $\mathcal{B}^{(3)}$ to order 40 for $w \in [0.35, 1.7]$ is sufficient for producing near
 631 machine-zero estimates. This implementation has been used for producing the results
 632 presented in Section 7.

- 634 [1] *The GNU Compiler Collection 10.3*. <https://gcc.gnu.org/onlinedocs/gcc-10.3.0>.
 635 [2] A. ABEDIAN, J. PARVIZIAN, A. DÜSTER, H. KHADEMYZADEH, AND E. RANK, *Performance of*
 636 *different integration schemes in facing discontinuities in the Finite Cell Method*, International
 637 Journal of Computational Methods, 10 (2013), p. 1350002, <https://doi.org/10.1142/S0219876213500023>.

- [3] P. ANTOLIN AND T. HIRSCHLER, *Quadrature-free Immersed Isogeometric Analysis*, July 2021, <https://arxiv.org/abs/2107.09024>.
- [4] S. BNÀ, S. MANSERVISI, R. SCARDOVELLI, P. YECKO, AND S. ZALESKI, *Numerical integration of implicit functions for the initialization of the VOF function*, Computers & Fluids, 113 (2015), pp. 42–52, <https://doi.org/10.1016/j.compfluid.2014.04.010>.
- [5] E. BURMAN, S. CLAUS, P. HANSBO, M. G. LARSON, AND A. MASSING, *CutFEM: Discretizing geometry and partial differential equations*, International Journal for Numerical Methods in Engineering, 104 (2015), pp. 472–501, <https://doi.org/10.1002/nme.4823>.
- [6] A. CHIERICI, L. CHIRCO, V. LE CHENADEC, R. SCARDOVELLI, P. YECKO, AND S. ZALESKI, *An optimized Vof library to initialize the volume fraction field*, Computer Physics Communications, (2022), p. 108506, <https://doi.org/10.1016/j.cpc.2022.108506>.
- [7] E. B. CHIN AND N. SUKUMAR, *An efficient method to integrate polynomials over polytopes and curved solids*, Computer Aided Geometric Design, 82 (2020), p. 101914, <https://doi.org/10.1016/j.cagd.2020.101914>.
- [8] R. CHIODI AND O. DESJARDINS, *General, robust, and efficient polyhedron intersection in the interface reconstruction library*, Journal of Computational Physics, 449 (2022), p. 110787, <https://doi.org/10.1016/j.jcp.2021.110787>.
- [9] L. DAGUM AND R. MENON, *OpenMP: An industry standard API for shared-memory programming*, IEEE Computational Science and Engineering, 5 (Jan.-March/1998), pp. 46–55, <https://doi.org/10.1109/99.660313>.
- [10] S. C. DIVI, C. V. VERHOOSEL, F. AURICCHIO, A. REALI, AND E. H. VAN BRUMMELEN, *Error-estimate-based adaptive integration for immersed isogeometric analysis*, Computers & Mathematics with Applications, 80 (2020), pp. 2481–2516, <https://doi.org/10.1016/j.camwa.2020.03.026>.
- [11] D. A. DUNAVANT, *High degree efficient symmetrical Gaussian quadrature rules for the triangle*, International Journal for Numerical Methods in Engineering, 21 (1985), pp. 1129–1148, <https://doi.org/10.1002/nme.1620210612>.
- [12] C. ENGWER, S. MAY, A. NÜSSING, AND F. STREITBÜRGER, *A Stabilized DG Cut Cell Method for Discretizing the Linear Transport Equation*, SIAM Journal on Scientific Computing, 42 (2020), pp. A3677–A3703, <https://doi.org/10.1137/19M1268318>.
- [13] M. EVANS AND T. SWARTZ, *Approximating Integrals via Monte Carlo and Deterministic Methods*, no. 20 in Oxford Statistical Science Series, Oxford University Press, Oxford ; New York, 2000.
- [14] G. E. FARIN, *From conics to NURBS: A tutorial and survey*, IEEE Computer Graphics and Applications, 12 (1992), pp. 78–86, <https://doi.org/10.1109/38.156017>.
- [15] G. E. FARIN, *Curves and Surfaces for CAGD: A Practical Guide*, Morgan Kaufmann Series in Computer Graphics and Geometric Modeling, Morgan Kaufmann, San Francisco, CA, 5th ed ed., 2001.
- [16] T. HAHN, *Cuba—a library for multidimensional numerical integration*, Computer Physics Communications, 168 (2005), pp. 78–95, <https://doi.org/10.1016/j.cpc.2005.01.010>.
- [17] E. HARTMANN, *\$G2\\$ interpolation and blending on surfaces*, The Visual Computer, 12 (1996), pp. 181–192, <https://doi.org/10.1007/BF01782321>.
- [18] T. HUGHES, J. COTTRELL, AND Y. BAZILEVS, *Isogeometric analysis: CAD, finite elements, NURBS, exact geometry and mesh refinement*, Computer Methods in Applied Mechanics and Engineering, 194 (2005), pp. 4135–4195, <https://doi.org/10.1016/j.cma.2004.10.008>.
- [19] B. W. JONES, A. G. MALAN, AND N. A. ILANGAKOON, *The initialisation of volume fractions for unstructured grids using implicit surface definitions.*, Computers & Fluids, 179 (2019), pp. 194–205, <https://doi.org/10.1016/j.compfluid.2018.10.021>.
- [20] W. KAHAN, *Pracniques: Further remarks on reducing truncation errors*, Communications of the ACM, 8 (1965), p. 40, <https://doi.org/10.1145/363707.363723>.
- [21] J. KROMER AND D. BOTHE, *Highly accurate computation of volume fractions using differential geometry*, Journal of Computational Physics, 396 (2019), pp. 761–784, <https://doi.org/10.1016/j.jcp.2019.07.005>.
- [22] J. KROMER AND D. BOTHE, *Third-order accurate initialization of VOF volume fractions on unstructured grids with arbitrary polyhedral cells*, arXiv:2111.01073 [cs, math], (2021), <https://arxiv.org/abs/2111.01073>.
- [23] L. KUDELA, N. ZANDER, S. KOLLMANNBERGER, AND E. RANK, *Smart octrees: Accurately integrating discontinuous functions in 3D*, Computer Methods in Applied Mechanics and Engineering, 306 (2016), pp. 406–426, <https://doi.org/10.1016/j.cma.2016.04.006>.
- [24] S. LODHA AND J. WARREN, *Bézier representation for quadric surface patches*, Computer-Aided Design, 22 (1990), pp. 574–579, [https://doi.org/10.1016/0010-4485\(90\)90042-B](https://doi.org/10.1016/0010-4485(90)90042-B).
- [25] Y. RENARDY AND M. RENARDY, *PROST: A Parabolic Reconstruction of Surface Tension for*

- 701 *the Volume-of-Fluid Method*, Journal of Computational Physics, 183 (2002), pp. 400–421,
702 <https://doi.org/10.1006/jcph.2002.7190>.
- 703 [26] R. SEVILLA, S. FERNÁNDEZ-MÉNDEZ, AND A. HUERTA, *NURBS-enhanced finite element method (NEFEM)*, International Journal for Numerical Methods in Engineering, 76 (2008),
704 pp. 56–83, <https://doi.org/10.1002/nme.2311>.
- 705 [27] S. J. TELLER AND C. H. SÉQUIN, *Modeling Implicit Quadrics and Free-form Surfaces With Trimmed Rational Quadratic Bezier Patches. and Carlo H. Séquin. (CSD-90-577)*, tech.
706 report, Computer Science Division, U.C. Berkeley, June 1990.
- 707 [28] T. TOLLE, D. GRÜNDING, D. BOTHE, AND T. MARIĆ, *triSurfaceImmersion: Computing volume
710 fractions and signed distances from triangulated surfaces immersed in unstructured meshes*, Computer Physics Communications, 273 (2022), p. 108249, <https://doi.org/10.1016/j.cpc.2021.108249>.
- 711 [29] G. TURK, *Stanford 3D Scanning Repository*. <http://graphics.stanford.edu/data/3Dscanrep/>,
712 1994.
- 713
- 714